JGR Planets

Retrieval of Martian Atmospheric CO Vertical Profiles From NOMAD Observations During the First Year of TGO Operations

Ashimananda Modak[1] , Miguel Angel López-Valverde[1] , Adrian Brines[1] , Aurélien Stolzenbach[1] , Bernd Funke[1] , Francisco González-Galindo[1] , Brittany Hill[1], Shohei Aoki[2] , Ian Thomas[3] , Giuliano Liuzzi[4,5] , Gerónimo Villanueva[4] , Justin Erwin[3] , José Juan Lopez Moreno[1], Nao Yoshida[6] , Udo Grabowski[7], Francois Forget[8], Frank Daerden[3] , Bojan Ristic[3] , Giancarlo Bellucci[9], Manish Patel[10] , Loic Trompet[3] , and Ann-Carine Vandaele[3]

[1]Instituto de Astrofísica de Andalucia, Granada, Spain, [2]Graduate School of Frontier Sciences, The University of Tokyo, Kashiwa, Japan, [3]Belgian Royal Institute for Space Aeronomy, Brussels, Belgium, [4]NASA Goddard Space Flight Center, Greenbelt, MD, USA, [5]American University, Washington, DC, USA, [6]Graduate School of Science, Tohoku University, Sendai, Japan, [7]Karlsruhe Institute of Technology, Institute of Meteorology and Climate Research, Karlsruhe, Germany, [8]Laboratoire de Météorologie Dynamique, IPSL, Paris, France, [9]Institute for Space Astrophysics and Planetology, Rome, Italy, [10]Open University, Milton Keynes, UK

Abstract We present CO density profiles up to about 100 km in the Martian atmosphere obtained for the first time from retrievals of solar occultation measurements by the Nadir and Occultation for Mars Discovery (NOMAD) onboard ExoMars Trace Gas Orbiter (TGO). CO is an important trace gas on Mars, as it is controlled by CO_2 photolysis, chemical reaction with the OH radicals, and the global dynamics. However, the measurements of CO vertical profiles have been elusive until the arrival of TGO. We show how the NOMAD CO variations describe very well the Mars general circulation. We observe a depletion of CO in the upper troposphere and mesosphere during the peak period, $L_S = 190°–200°$, more pronounced over the northern latitudes, confirming a similar result recently reported by Atmospheric Chemistry Suite onboard TGO. However, in the lower troposphere around 20 km, and at least at high latitudes of the S. hemisphere, NOMAD CO mixing ratios increase over 1,500 ppmv during the GDS (Global Dust Storm) onset. This might be related to the downwelling branch of the Hadley circulation. A subsequent increase in tropospheric CO is observed during the decay phase of the GDS around $L_S = 210°–250°$ when the dust loading is still high. This could be associated with a reduction in the amount of OH radicals in the lower atmosphere due to lack of solar insolation. Once the GDS is over, CO steadily decreases globally during the southern summer season. A couple of distinct CO patterns associated with the Summer solstice and equinox circulation are reported and discussed.

Plain Language Summary CO is an extremely interesting trace species in the Martian atmosphere. It has been used for both dynamical and photochemical studies of the atmosphere. But its vertical distribution has not been systematically measured until the arrival of the Exomars Trace Gas Orbiter (TGO). We use observations of the NOMAD (Nadir and Occultation for Mars Discovery) spectrometer onboard TGO to retrieve full profiles of mixing ratios of CO up to 100 km with a good vertical resolution. The retrievals cover two Martian seasons during which a global dust storm event occurred. We have found the behavior of CO during this event to be governed by local chemistry as well as by the long range transport. During the dust storm, CO mixing ratios are depleted all over the globe while over the southern high latitudes, we discover an increase in CO due to transport from low latitudes during the end of the southern winter. The dynamical effect of global transport is found in the vertical distribution of CO during the southern summer. Another important result, where the local chemistry might be at play is the increase of CO in the low altitudes over low and midlatitudes during the decay phase of the GDS.

1. Introduction

CO is a trace gas of large interest in the Martian atmosphere as its distribution is ruled by photochemistry and dynamics. It is produced in the upper atmosphere of Mars by photolysis of CO_2 and destroyed in the lower atmosphere by the hydroxyl radicals (OH) (McElroy & Donahue, 1972; Parkinson & Hunten, 1972). Due to the long photochemical lifetime of CO in the Martian atmosphere (González-Galindo et al., 2005) it can be used as a

dynamical tracer. As a noncondensable gas, CO shows strong variations in the polar regions during sublimation and condensation of the polar caps and a slow seasonal variation in the low-latitude region (Forget et al., 2008). The CO density can also be used to constrain dynamical parameters of models such as eddy diffusion coefficients in the homosphere (Rodrigo et al., 1990; Yoshida et al., 2022).

CO on Mars was first detected from Earth by Kaplan et al. (1969) using high resolution infrared Fourier spectroscopy. Later, ground based observations used infrared (Billebaud et al., 1991), microwave (R. Clancy et al., 1983; Kakar et al., 1977), millimeter (Lellouch et al., 1991), and submillimeter (Encrenaz et al., 1991) spectroscopy. In more recent ground based efforts, a positive north-to-south gradient of CO column averaged mixing ratio was found in latitudinal mapping during summer (Krasnopolsky, 2015) and an opposite trend was found during winter (Krasnopolsky, 2003). These ground based observations showed an average CO volume mixing ratio (VMR) around 800 ppmv, with significant seasonal and latitudinal variability.

Other instruments dedicated to the study of CO in the Mars' atmosphere are PFS (Planetary Fourier Spectroscopy) and OMEGA (Observatoire pour la Minéralogie, l'Eau, les Glaces et l'Activité) onboard MEX (Mars EXpress) (Encrenaz et al., 2006), CRISM (Compact reconnaissance imaging spectrometer for Mars) onboard MRO (Smith et al., 2009), and LNO (Limb Nadir Occultation) of NOMAD (The Nadir and Occultation for MArs Discovery instrument) onboard TGO (Trace Gas Orbiter) (Smith et al., 2021). All these instruments have significant coverage in both latitudes and seasons and have been operating for several years. Recently, PFS measurements for 7 Martian years were used to study the seasonality of CO from the nadir observations (Bouche et al., 2021). Another significant result found from the PFS observations is the low values of CO VMR (Sindoni et al., 2011) during the perihelion season from high southern latitudes to 50°N. In another study from the PFS observations, high constant values (1,200 ppm) of the CO column is found during $L_S = 330°–360°$ (Billebaud et al., 2009). OMEGA measurements reveal the seasonal behavior of CO over the Hellas basin (Encrenaz et al., 2006) where CO mixing ratios increase by a factor of 2 during winter. These results from PFS and OMEGA indicate the seasonal and topographical effect on column abundance of CO. A more detailed study of CO column with seasonal and spatial variations was performed with the measurements from CRISM (Smith et al., 2009). These studies confirm depletion of CO due to the sublimation of polar ice, a behavior predicted by Ar distribution observed by the Gamma Ray Spectrometer (GRS) onboard Mars Odyssey spacecraft (Sprague et al., 2004) and the Mars Global Climate Model developed at the Laboratoire de Météorologie Dynamique (LMD-MGCM) (Forget et al., 2008), which is now known as Mars Planetary Climate Model (Mars PCM) (Forget et al., 2022). CRISM measurements also show a weak correlation of CO with surface pressure in the low latitude region (Smith et al., 2018).

From the above mentioned ground-based and space borne measurements, we know a great deal about the variation of the column averaged CO and its qualitative relation with the seasonal pressure cycle. Very recently, column averaged mixing ratio of CO is reported by Smith et al. (2021) from the LNO measurement of NOMAD. They have established a global average of 800 ppm. This revealed that CO seasonal variation is greater in the polar regions than at the equator. The column measurements are mostly representative of the surface CO VMR. However, in order to characterize its dynamical and chemical sources and sinks, and underlying atmospheric variability, the density measurements are necessary. For example, a recent study of the variation of Martian CO obtained from the MIR (midinfrared) channel of ACS (Atmospheric Chemistry Suite) onboard TGO found that CO is depleted during the MY 34 global dust storm (GDS) (Olsen et al., 2021). The seasonal coverage used in Olsen et al. (2021) was limited. An extended set of measurements from ACS but with a different spectral channel (NIR, near-infrared) is included in this special issue (A. Fedorova et al. (2022)) which includes comparisons with the measurements of MIR and TIRVIM.

Until the arrival of TGO, the empirical description of Martian CO density profiles, with a good resolution in the vertical and in a systematic manner, was essentially absent. Here, we present vertical profiles of CO retrieved from the measurements recorded by NOMAD solar occultation (SO) for the first year of TGO observations from April 2018 to March 2019, for the first time. This covers the last two seasons of MY 34 with fine latitudinal coverage. The characteristics of the chosen data set corresponding to these observations are described in Section 2 along with a brief description of the NOMAD SO channel. Section 3 is dedicated to the preparation or cleaning steps of the data analysis before they are used by our retrieval scheme. The retrieval scheme is described in detail with an example of a scan retrieval in Section 4. Results of the CO retrieval from the above mentioned data set are presented in Section 5, where we describe the seasonal, latitudinal, and diurnal variation in the CO distribution. The next section also includes a proper comparison of the results with the model predictions.
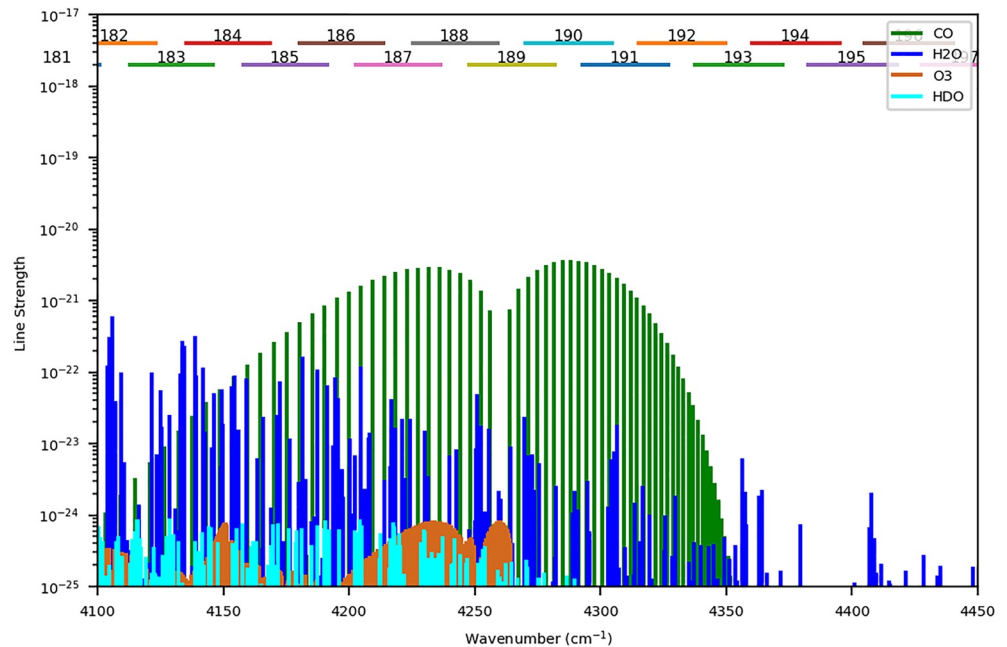
Figure 1. Spectral location of Nadir and Occultation for Mars Discovery solar occultation diffraction orders for CO and other atmospheric species with indication of strength of the strongest ro-vibrational absorption lines. The positions and line strengths are from HITRAN 2016 (Gordon et al., 2017).

2. The NOMAD Instrument and Data Set

NOMAD is a suite of three spectrometers onboard ExoMars TGO. Two spectrometers operate in the infrared (IR), the SO and the LNO. A third spectrometer, UVIS (The Ultraviolet and Visible Spectrometer), operates in the ultraviolet and visible (Vandaele et al., 2015, 2018). SO performs SO and LNO performs both limb scanning and nadir observation. The UV spectrometer is capable of scanning the Mars atmosphere both in SO and nadir viewing mode (Patel et al., 2017). In this work, we will analyze data from the SO channel. This channel covers a spectral range 2.2–4.3 μm and it has a nominal resolving power of 20,000 (Neefs et al., 2015). NOMAD SO uses an echelle grating in Littrow configuration which means the incident, reflected, and Blaze angles are equal for this configuration (Neefs et al., 2015). The other components of the SO channels are the detector, parabolic mirrors, and Acousto Optical Tunable Filter (AOTF). The NOMAD SO detector has 320 columns for the spectral dimension and 256 for the spatial dimension. The AOTF acts as a band-pass filter controlled by radio frequency input. Ideally, it selects one wavelength range for a radio frequency input and sends it to the grating through parabolic mirrors, and diffracted light falls on the detector after being guided by the parabolic mirrors. The wavenumber range limit of the AOTF is adjusted to ideally capture only one diffraction order at a time. In practice, adjacent diffraction orders do overlap and in the case of NOMAD SO (see Section 3), this adds non-negligible components which need to be taken into account in the forward model (Liuzzi et al., 2019; Villanueva et al., 2022). A quantitative description of this contamination for the CO orders used in this work is presented below in Section 3. Once the diffraction order is selected, the incoming radiation is dispersed through the grating and incident on the detector's pixels. The intensity distribution of the diffraction order depends on the AOTF transfer function and the blaze function (Liuzzi et al., 2019). The blaze function characterizes the diffraction efficiency of grating depending on the wavelength. These two functions, that is, the AOTF transfer function and the grating blaze function need to be very well characterized in order to simulate the NOMAD measured radiance correctly. For the complete optical description of the SO channel, one can refer to Neefs et al. (2015).

The NOMAD diffraction orders suitable for CO retrievals are shown in Figure 1, together with line positions from HITRAN 2016 (Gordon et al., 2017). In the NOMAD SO spectra, the CO rotational-vibrational lines are well separated and there is no significant absorption from other atmospheric species such as H_2O, CO_2 in the orders between 186 and 191. The H_2O lines are shown for comparison purposes only; they are much weaker than the CO lines and are not observed in the NOMAD data. We choose order 190 for the retrieval because some of the

strongest CO absorption lines lie in this order. Also, the number of atmospheric scans performed by NOMAD SO is much larger than in any other diffraction order during the first year of operations.

3. Data Cleaning and Preprocessing

In this work, we use NOMAD Level 1 calibrated transmittances. These are downloaded as formatted data and provide values of atmospheric transmittances, measurement noise, and calibration parameters such as the parameters for the pixel to wavenumber conversion, the center of the blaze function, etc. We first clean these transmittances from diverse systematics such as spectral bending and shift (see Section 3.2) before ingesting it into the actual inversion scheme. We call this internal step preprocessing and it is described below in Section 3.2. Both preprocessing and retrieval make use of a line-by-line forward model, central to our analysis, which is described next.

3.1. The KOPRA Forward Model

We use the Karlsruhe Optimized and Precise Radiative transfer Algorithm (KOPRA) described in Stiller (2000), to simulate the NOMAD SO measurements, both during the "data cleaning" phase and at the core of the inversion processor. KOPRA has been widely used for the retrievals of Earth atmospheric gases and aerosols (Höpfner & Emde, 2005; Schreier et al., 2018). KOPRA solves the radiative transfer (RT) equation in a line-by-line approach to calculate monochromatic radiance. In our adaptation to Mars SO conditions, the atmosphere is divided into layers of 1 km width from the ground to 60 km, layers of 2 km from 60 to 90 km, 2.5 km from 90 to 130 km, and 5 km from 130 to 220 km. The RT calculations are done along the line of sight of the observations. The model calculates the line absorptions from the spectroscopic information provided by the HITRAN 2016 database (Gordon et al., 2017).

The instrumental line shape (ILS) of the NOMAD SO is one of the essential parameter for atmospheric retrievals as it reflects the manner in which the spectra are recorded across the detector (Aoki et al., 2021; Liuzzi et al., 2019; I. R. Thomas et al., 2022). The NOMAD SO instrumental response, including the AOTF and the ILS have been the subject of a recent revision, and we use a parameterization from a consolidated approach in collaboration with various teams within the NOMAD consortium (Villanueva et al., 2022). The ILS is parameterized as double Gaussian function. Its peaks, widths, and the distance between the Gaussian functions for every order have been determined combining several analytical and retrieval methods. The variability of the ILS within each order and across orders is a NOMAD-SO specific difficulty which we consider as well characterized, as can be seen from inspection of the retrieval's residuals. However, for the AOTF transfer function, its parameterization is further fine-tuned around the values suggested by Villanueva et al. (2022). This fine-tuning is described in Appendix A, and permitted a significant improvement in the retrievals. We convolved the KOPRA spectra with the revised ILS, the fine-tuned AOTF, and the blaze function (Brines et al., 2022). This convolution is done within the forward model.

3.2. Preprocessing

An example of NOMAD calibrated transmission data from one particular scan in diffraction order 190 is shown in Figure 2, panel a. Recorded against pixel number, transmittances are transformed into wavenumber dependent function during the nominal calibration, using a second order polynomial relation between wavenumber and pixel number (Liuzzi et al., 2019). The different colors correspond to different tangent heights, and the vertical lines in red indicate the position of the center of the CO rotational-vibrational lines for the main order 190. The transmittances clearly suffer from spectral shift and bending of the continuum across the detector (Figure 2, panel a) which occurs due to thermally induced mechanical stress on the detector Liuzzi et al. (2019). This bending effect is almost ubiquitous, present in all NOMAD orders at all altitudes and scans (Vandaele et al., 2018). It changes from each altitude to the next in a quasi-random manner and systematically responds to a (variable) 4th order polynomial. Notice that this is very different to the atmospheric continuum due to aerosols absorption, which can be considered as spectrally constant due to the narrow span of the NOMAD orders (Vandaele et al., 2018) and which is usually important at low altitudes.

Before using these data in a proper inversion of densities they need to be corrected for these two effects. For this purpose, the NOMAD transmittances are divided into small microwindows (MW) containing at least one
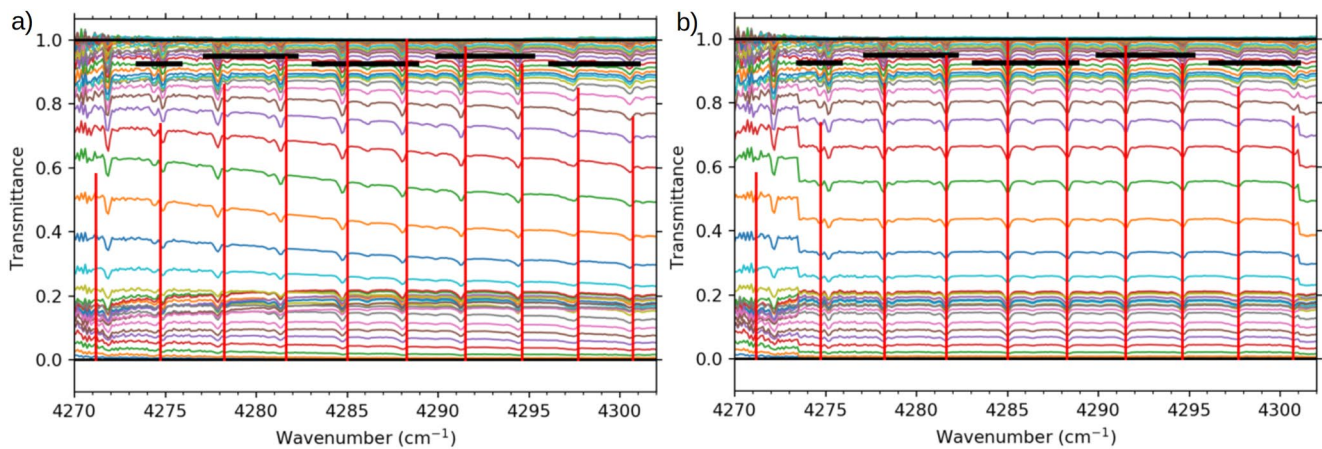
Figure 2. Example of our cleaning method applied to diffraction order 190 in one specific scan (20180503_151030_SO_A_E). Panel (a), all the original spectra (calibrated transmittances) taken in this scan, showing clear bending effects and spectral shifts. Panel (b), spectra after cleaning. Notice the cleaning is only applied to a subset of the full diffraction order. Vertical red solid lines indicate the expected position of the CO spectral lines (HITRAN 2016). The five short horizontal lines in black near the top of the panels indicate the microwindows used for this cleaning. See text for details.

absorption line (see Figure 2). The spans of these MWs are shown in Figure 2 and are 4,273.50–4,275.80, 4,277.20–4,282.200, 4,283.2–4,288.80, 4,290.00–4,295.20, and 4,296.20–4,301.00 cm^{-1}.

Starting with the bending effect, in all NOMAD orders this is usually very small in the central part of the order. In each order it is corrected using a polynomial fitting to the background continuum or baseline, as simulated with KOPRA at each tangent altitude. This correction is used as a multiplicative factor because the ultimate reason for this effect comes from small changes in the AOTF response during each SO scan. This explains the spectrally low variation (4th polynomial) in the spectra. During these changes the AOTF varies very little in the center of the order, where it is essentially one. Therefore the effect on the measured radiances should be multiplicative, and consequently, also on the transmittances. The use of a line-by-line calculation at each altitude to correct for the bending guarantees that the effect from gas line-overlapping is taken into account and is separated from the actual bending effect. Still, this correction may be a source of uncertainty for the retrieval of aerosol properties, and a simple strategy to minimize this is to select the center of the order to derive them at each altitude.

Regarding the spectral shift, present in all spectra, that is, at all altitudes, and variable from scan to scan, this is determined from comparisons of data and model simulations at all altitudes with significant line absorption (to minimize errors during its determination). These spectral shifts, as it also occurs in other diffraction orders, vary across the order in a linear manner. A linear function is fitted on the values of the shifts obtained for each MW, and this is interpolated across the wavenumber range of the spectra for a full-order correction. Microwindows near the edge of the order are not considered due to higher noise there. Details of these corrections are presented in a companion paper in this special issue (López Valverde et al., 2022).

Our inversion scheme uses radiances instead of transmittances. Thus the cleaned Level-1a transmittances are converted into solar radiances using a space view simulation with KOPRA, at 220 km tangent altitude, using the AOTF appropriate for this diffraction order and the grating properties described by the blaze function (Liuzzi et al., 2019). The space view radiance is calculated using a reference solar radiance supplied externally. This reference radiance has no other function and has no impact on the inversion.

One additional caution, related to the MWs selection, deserves some discussion. As mentioned before, one characteristic of real AOTF spectrometers is that the addition of adjacent diffraction orders to the main order is not negligible. These contributions, when added to the forward model, guided the selection of the MWs in this study (Villanueva et al. (2022) also see Appendix A). Figure 3 shows one example of this contamination by adjacent orders in the case of order 190. The vertical lines in the plot indicate the positions of CO absorption lines from different adjacent orders. The main order is indicated with the solid red color and the adjacent orders on both sides with the same color but with a solid line on the left and with a dotted line on the right. Three central absorption lines of the spectra within 4,285 and 4,292 cm^{-1} are not at all contaminated with the
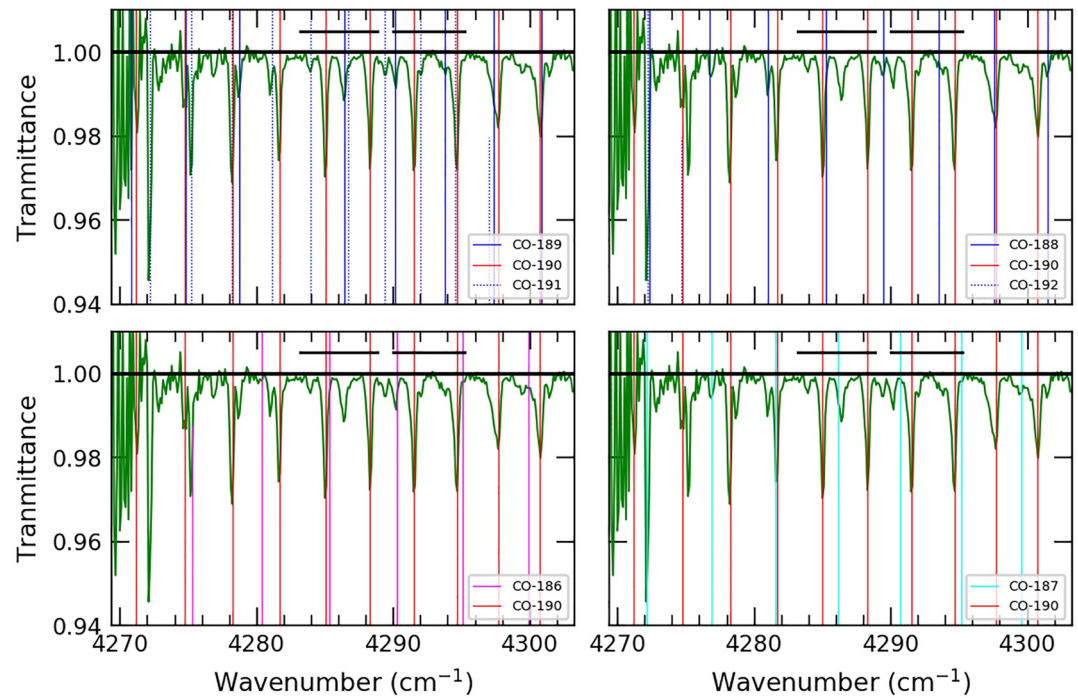
Figure 3. Example of contamination from the four adjacent orders at each side of the principal diffraction order 190. Colored vertical lines represent the position of the CO absorption present in the different orders as indicated in the legends. Four panels are used for clarity, showing different adjacent orders in each of them versus the central order 190. The selected microwindows for the inversion are shown in thick black horizontal lines. See text for details.

absorption from the adjacent orders. As can be seen from Figure 3 most of the contaminations are from orders 187, 188, and 189 on the left and 191 on the right. A maximum of four orders contamination to either sides is shown in Figure 3, which is sufficient to explain the absorption line in the diffraction order 190. This contamination, in addition to line strength considerations, was taken into account during the selection of the MWs used in this work. For the inversion of CO (next section) we finally selected two MWs near the center of the order, shown in Figure 3.

4. Retrieval Scheme

After the cleaning of the Level-1a transmission data described above, we performed the CO retrieval using an inversion processor called Retrieval Control Programming (RCP) described in von Clarmann et al. (2003). We summarize here some of its characteristics. Our global-fit retrieval scheme and application are common to other NOMAD retrieval targets at the IAA team, including H_2O (Brines et al., 2022), temperature and CO_2 densities (López Valverde et al., 2022), all in this special issue.

RCP uses KOPRA as its forward model and follows a usual iterative approach to solve the inverse solution to the RT equation, based upon a Levenberg-Marquardt least square minimization algorithm. RCP can use diverse solution methods, like an optimal estimation approach, but in this work, we use a more flexible first order Tikhonov regularization. In each iteration, it runs KOPRA and the simulated spectra are compared to the measured ones at each altitude simultaneously until convergence is reached when the variation in the target quantities are smaller than a fraction of the noise error (Jurado Navarro, 2016). RCP also provides averaging kernel (AK) and noise error for the target. The AK is expressed as $A = GK$ where G is the gain matrix and K is Jacobian matrix (Rodgers, 2000). The gain matrix is defined in Rodgers (2000) as follows:

$$G = \left(K^T S^{-1} K + R \right)^{-1} K^T S_y^{-1}. \tag{1}$$

K is the Jacobian matrix, S_y is the covariance matrix for the measurement noise, and R is the regularization matrix. The value of the AK is always below unity. The noise error is mapped onto the retrieval grid as defined in the equation below:

$$S_x = G^T S_y G. \tag{2}$$

The χ^2 is defined as follows:

$$\chi^2 = (y - F(x))^T S_y^{-1}(y - F(x)) + (x - x_a)^T R(x - a), \tag{3}$$

where y is the measurement, $F(x)$ is the forward model, x_a is the a priori state vector, and x is the true state vector which includes our target CO abundance profile. The retrieval of CO with our retrieval scheme is found to be robust against large variations in the a priori values of CO (see Appendix B).

The a priori CO profiles extended from the planet's surface up to 200 km and are obtained from the Mars PCM (Forget et al., 1999; Lefèvre et al., 2021) using the dust scenarios for MY 34 and MY 35 (Montabone et al., 2015, 2020). The model uses dust and water cycles described in Navarro et al. (2014). The model outputs are at defined grids and are interpolated to the time and location of the NOMAD SO observation. The atmosphere needed by the forward model is built using the pressure and temperature retrieved from SO observation of diffraction order 149 (López Valverde et al., 2022).

In a typical CO VMR profile retrieval, RCP performs the simultaneous inversion of three quantities or targets, the CO VMR, a spectral shift, and a baseline accommodating factor named scale-h. The shift is used as a target with the intention to detect any residual spectral shift remaining after the correction already performed at the preprocessing level. Scale-h is a spectrally constant transmittance level within each MW, adjusted to account for the impact of aerosol absorption on the continuum and any small remaining calibration biases in each MW. As mentioned above, the continuum absorption within the narrow NOMAD diffraction orders is spectrally flat (Vandaele et al., 2018) but with this Scale-h parameter, we allow for small variations between MWs.

Before the actual application to real measurements, an extensive study of synthetic retrievals, generated using KOPRA, was performed. These were very useful to test the performance of the inversion, its independence on a priori assumptions and to fine-tune the regularization. Appendix B presents some details and results from the synthetic retrievals.

4.1. Typical Retrieval Performance

To illustrate the performance of an inversion scheme, it is of paramount importance to examine the residuals or best fit obtained and to characterize the error propagation and vertical resolution by an analysis of the AKs.

An example of the best fit spectrum achieved with our inversion scheme is shown in the upper panel of Figure 4, for one particular scan and a tangent altitude of 74 km. Figure 4 also shows the spectrum generated with the a priori CO profile, for comparison. The lower panel depicts the residual transmittances (at the end of the iteration and convergence) together with the model-data difference when using the a priori. The best fit residual transmittance spectrum lies within the limit of the measurement noise at all wavenumbers.

Figure 5 shows a set of typical diagnostics for the scan in Figure 4. From left to right, the four panels show the retrieved CO profile, the rows of the AK, the percentage error at each altitude, and the vertical resolution profile, respectively. The AK shows the mapping of the measurements onto the retrieval grid. The vertical resolution is the usual interpretation of the full width at half maximum of the AK at each retrieval altitude. The CO VMRs retrieved in this example are greater than the a priori (shown in red), specially above 60 km. The errors are typically within 10%–15% below 80 km. The vertical resolution is within 5 km in the region below 80 km and increases with altitude, as the measurement noise and the retrieval error also do. The shaded region below 28 km, in the first panel, indicates the altitude where the slant optical depth is larger than 1.5. We do not retrieve CO in the altitudes with high dust opacities to avoid biases from the severe contamination in (reduction of) the spectral absorption lines. For such spectra, the AK values obtained in the retrieval diagnostics are zero, corresponding to no information.

After few experiments, we make use of a minimum value (0.03) of the AK. Retrieved CO densities with AKs below this minimum are not trusted. All the results presented in this study are qualified by this condition.
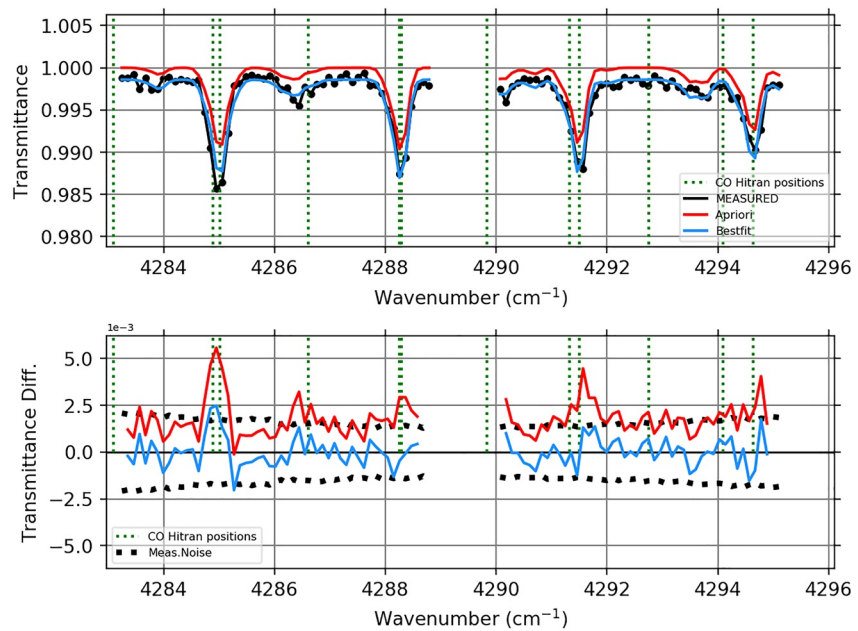
Figure 4. Best fit spectrum to the Nadir and Occultation for Mars Discovery (NOMAD) cleaned transmittances at a tangent altitude of about 74 km from scan 20180801 055956 solar occultation (SO) A E 190 (Lat 66°N, Lon 161°W, Ls 222°). The top panel shows the measured spectrum in solid black line with dots, the best fit spectrum at the end of the inversion is blue, and the spectrum obtained with the a priori atmospheric profile in red. The spectrum is split in two segments which correspond to the 2 MWs used in the inversion. The lower panel shows the residuals (Model fit–NOMAD) in blue, together with the same quantity but calculated with the model spectrum for the a priori atmosphere, in red. The dotted lines represent the NOMAD SO measurement errors used in the inversion.
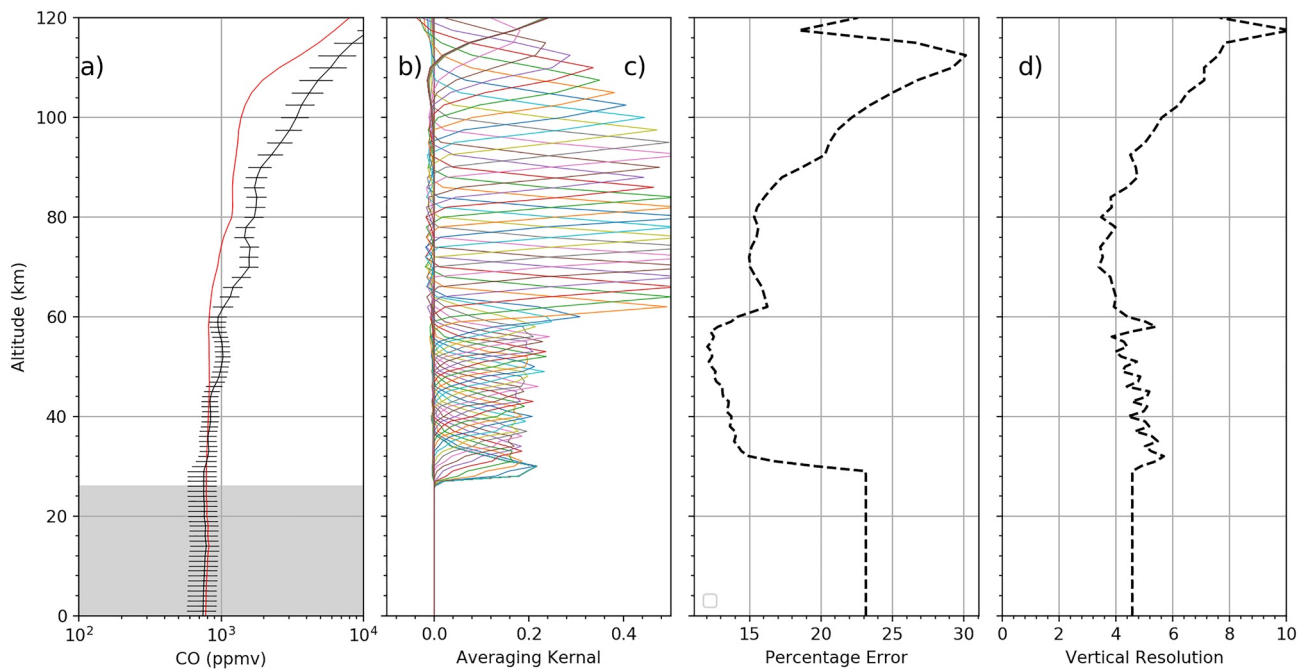

Figure 5. Retrieved CO profile from the same scan as in Figure 4 with error bars (panel a). The red line is the a priori profiles, the black line is the retrieved CO. The shaded area below 28 km represents the region of very high dust loading, where the solar occultation spectra are not inverted. Panel (b) selected rows of the averaging kernel (AK) matrix; the sharp change in the peak of the AK at 60 km is due to the change in the retrieval grid (see Section 3.1 for the retrieval grid definition). Panel (c) percentage error in the CO profile. Panel (d) Vertical resolution, as given by the widths of the AK rows.
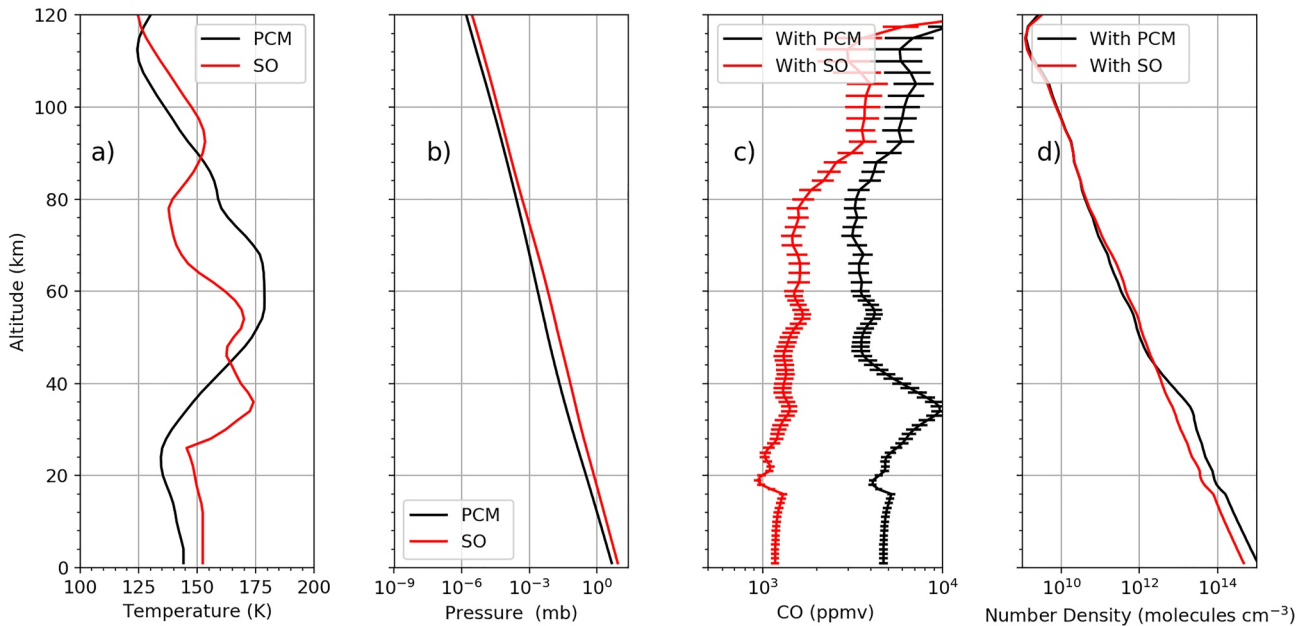
Figure 6. The effect of the reference thermal structure on the retrieved CO. Panel (a) Temperature profiles from Planetary Climate Model (PCM) (black line) and from Nadir and Occultation for Mars Discovery (NOMAD) retrievals in order 149 (red line). Panel (b) Pressure profiles from PCM (black) and from NOMAD (red). Panel (c) retrieved CO volume mixing ratio using the PCM inputs (black line) versus the NOMAD retrievals (red lines). Panel (d) Same as Panel (c) but for the CO local number density (cm^{-3}).

Figure 5, panel b shows the diagonal of the AKs for a typical NOMAD SO scan and we observe that below about 80 km and down to 60 km these peaks are basically constant and they show small trend, with decreasing values below 60 km. This slow decrease in the AK could be indicative of line saturation. The lines used in order 190 are among the strongest in the IR spectrum. We made a study of the line depths in these limb geometry data in a small number of SO scans. This study show us that the saturation effect in the line absorption start below about 80 km and becomes stronger. However, our forward model is a state-of-the-art line-by-line RT code that reproduces well the saturation effects in the line absorption. In the case of saturated absorption lines, the information is mostly derived from the wings of the absorption lines, because the line depth at the line center does not vary with the increasing CO density. How much information can be extracted, that is, how large is the sensitivity to the CO density, is provided by the AKs.

4.2. Effect of Climatology on Retrieved CO

We studied the effect of the a priori temperature, by using the PCM as a reference and adding ad hoc perturbations on this profile. Here, we discuss one example, for scan 20180423_204351_1p0a_SO_A_I_190. Figure 6 shows two retrievals from the same SO scan using two sets of pressures and temperatures. The profiles in black correspond the a priori obtained from the PCM. The red lines correspond to the retrieval using as a priori the *T/P* profile obtained from the inversion of this NOMAD SO scan (in diffraction order 149, results obtained by López Valverde et al. (2022)). The retrieved CO VMR and absolute number densities in the two cases are shown in panels c and d, respectively. The obtained NOMAD pressures are higher than the PCM ones at each altitude, which in turn, results in a lower VMR than when using the PCM. The absolute CO density should be more independent of the densities assumed than the CO VMR, and this indeed observed above 50 km. But this is not the case of its dependence on the temperatures. And, we observed in panel (d) that the CO absolute densities are varying with the assumed temperatures, with a crossing point around 45 km tangent height, which is present in both temperature and retrieved CO. Since this temperature effect is very important, in this work, we only used scans for which retrieved NOMAD temperatures are available (from a parallel effort in our team, see companion paper on temperature retrievals led by M. A. Lopez-Valverde in this special issue). In other words, we only considered the subset of NOMAD SO scans where orders 190 and 149 were measured simultaneously, and the final set consists of those where the temperature converged, which is a very high percentage of the available scans (López Valverde et al., 2022). This is done regardless of the difference between the a priori and the retrieved thermal structure.
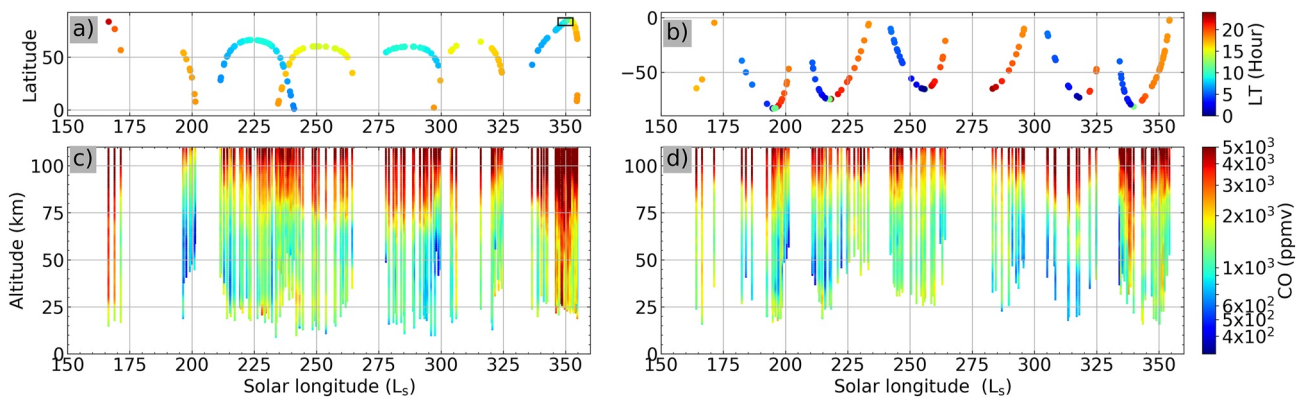
Figure 7. All CO profiles retrieved for this study. Panels (a) and (b) show the seasonal and latitudinal distribution of the data set used, with the colors on scale indicating the local time. The bottom panels show L_S-altitude distribution of the CO profiles corresponding to the location shown in the top panels. Colors are selected to facilitate inspection of iso-contours, like the orange iso-contour of 2,500 ppm, which varies through the seasons (see text for details). A box has been included in panel (a) to indicate the position of the data selected for the study of local time effects (see text).

5. Results and Discussion

The results of all our retrievals are shown in Figure 7. Due to the large variation in the CO relative abundance with altitude, we show the CO VMR values in log scale. The data set extends from $L_S = 160°$ to $L_S = 354°$ (Figure 7, panels a and b) covering important seasons such as the onset of the GDS ($L_S = 190°$) (Guzewich et al., 2019), the GDS decay phase ($L_S > 235°$), the end of the southern spring ($L_S = 245°$–263°), and the whole of the southern summer. In this section, following López Valverde et al. (2022), we refer to the atmospheric region from the surface up to 50 km as troposphere and to that above as mesosphere.

5.1. Seasonal Variation of CO

CO is a long lived gas species affected by the general circulation in the Martian atmosphere and therefore an excellent tracer of the global dynamics on Mars (Lefèvre & Krasnopolsky, 2017). Figure 7 permits some insight into the seasonal variation of the CO VMR; panels c and d show the CO VMR distribution over the northern and southern hemispheres (SHs), respectively. In general, and in agreement with PCM simulations, we observe a CO VMR increasing with altitude in the upper troposphere and through the mesosphere, as a result of the downward mixing from the CO source region at high altitude, following CO_2 photodissociation (González-Galindo et al., 2009; Krasnopolsky, 1995; Modak et al., 2020). Particularly large values and gradients are observed above about 60 km but with significant variations. This variability can be better visualized by inspecting a given CO VMR iso-contour in Figure 7, like the value of 2,500 ppmv (in orange color). This value is arbitrary but serves as a marker between two altitude regions with different physics regarding CO; the upper one driven by photochemical production and the lower one dominated by CO losses. CO VMR values as large as 2,500 ppmv occur very high in the atmosphere at midlatitude and low latitude, following CO_2 photodissociation, but can be seen at much lower altitudes toward the poles due to global dynamics, as discussed below in Section 5.2. This iso-contour is therefore particularly useful to illustrate the CO variability, both with season and latitude. Panels a and b show the track of the SO, where this mix of changes with season and latitude can be seen. Latitude has a large impact, different in the north and south hemispheres since the coverage of high latitudes is different in each hemisphere. Over the southern high latitudes the occultation spent less time which produces sudden changes in the iso-contour. As we discuss below in Section 5.2, it is possible to decouple the latitudinal and seasonal trends to study only one of these, for example, latitudinal variation for a small seasonal period.

There are two essential and different seasons where the dynamical behavior of the Martian atmosphere is distinct, the equinoxes and the solstices. So, we analyze here the CO distribution in these two periods and also its variability in between. During the northern autumn equinox period ($L_S = 160°$–180°) when two Hadley cells extend from the equator to high latitudes (Forget et al., 1999) and the solar insolation is similar in both hemispheres, we expect similar CO mixing ratios at similar latitudes in the north and south. And this is apparently the case in Figure 7, although unfortunately, only a few NOMAD scans are available during that period. For example,

over the northern high latitudes (>60°N) high values (~1,500 ppm) of CO VMRs are observed down to 20 km. Similar values of CO are also observed over the southern latitude 60°S.

The appearance of the MY 34 GDS in 2018 perturbed the global circulation and we expect the CO distribution to depart from what should be its regular seasonal cycle. We observe in Figure 7 that during the onset of the GDS in the period $L_S = 190°$ to $L_S = 205°$, the high altitude VMRs decrease (when looking at a fixed altitude, specially in the mesosphere). This shows the well-known tropospheric warming by solar heating of aerosols and the associated upward expansion in atmospheric density, moving our iso-contour of 2,500 ppm up to 100 km in the NH (northern hemisphere) during the GDS peak ($L_S = 205°$). Over the southern polar latitudes, however, the aerosols amount were lower, and that CO VMR iso-contour can be seen around 75 km.

After the onset of the GDS, the 2,500 ppmv iso-contour shows a CO VMR quickly increasing at all mesospheric altitudes in the NH until $L_S \sim 225°$. During the GDS, the high dust loading warms (and expand) the atmosphere which, in turn, reinforces the hemispheric Hadley cells. This increased circulation, has been shown to transport trace gases up to mesospheric altitudes (R. T. Clancy et al., 2010; Neary et al., 2020; Shaposhnikov et al., 2019; Vandaele et al., 2019). Since $L_S \sim 225°$ until about $L_S \sim 282°$ the iso-contour stays approximately constant at 70 km tangent height. Surely the first part of this period is dominated by the decay phase of the GDS while the second may be more typical of a seasonal behavior, that is, typical of a non-GDS year. The time evolution of the mesospheric CO VMR over SH at midlatitudes does not show those two different periods after the GDS. We observe a steadily small decrease with time up to about $L_S = 300°$. Our iso-contour is located at higher altitudes than in the NH, which shows an interhemispheric asymmetry, specially evident around the southern summer solstice, $L_S = 270°$. At the end of the southern summer, after $L_S = 330°$, the CO VMRs increase all over the globe, in both hemispheres. This increase is particularly noticeable at tropospheric altitudes.

The distribution of CO VMRs below 50 km reflects a completely different seasonal variability because it is not directly affected by CO_2 photolysis. During the onset of the GDS, CO mixing ratios are depleted at these altitudes. A similar depletion is also reported by Olsen et al. (2021) from ACS MIR observations. This depletion returned to possibly normal equinoctial abundances after the GDS, until in the southern summer another depletion of CO VMR occurred, around $L_S = 270°–300°$ (uncertain start in our records due to the lack of TGO observations around $L_S = 265°–280°$). This occurred in both hemispheres. Although these two periods share a drop in CO VMR, they may not respond to exactly the same processes. The well-known increase in CO_2 density in the southern solstice, during the sublimation of the southern polar cap (Forget et al., 2008; Hess et al., 1979), is surely behind the low CO observed after $L_S = 280°$. However, another mechanism may be at play during very dusty conditions. During the GDS and its decay phase high water vapor abundance has been reported (Alday et al., 2021; Belyaev et al., 2021; Brines et al., 2022; A. Fedorova et al., 2021; Villanueva et al., 2021). This suggests a depletion of CO due to enhanced H_2O which increases the hydroxyl radicals (OH).

At the lowermost altitudes explored, around 20–30 km, the retrieved CO shows large VMR after the GDS in the NH. This increase seems to disappear through the decay phase and is not observed around $L_S = 270°$. In the SH, however, the SO measurements during the onset of the GDS coincides with higher latitudes and a high CO abundance is also seen. This may also disappear as the season advances, but this is not confirmed as our data coverage is incomplete at these low altitudes. Let us bring up here that at the lowermost altitudes the CO sensitivity of our inversion is lower, and climatological effects (a priori) may play a role.

At the end of the southern summer, during $L_S = 335°–354°$, the CO VMR increases at high latitudes in both hemispheres. This enhancement is due to the downwelling branch of the equinoctial hemispheric Hadley cells (Forget et al., 1999; Neary & Daerden, 2018). This enhancement in CO is consistent with a higher column abundance observed in a nadir geometry by the NOMAD LNO channel (Smith et al., 2021).

5.2. Latitudinal Variation

In Figures 8 and 9, we show the latitudinal variation of the CO profiles retrieved from NOMAD-SO and simulated with the PCM, respectively. The CO mixing ratios simulated by the Mars PCM are shown in order to illustrate both the departure from the a priori and the predicted dynamical effects on the distribution. According to the PCM simulation, two Hadley cells exist, rising air from the equator and moving to high latitudes in both hemispheres during the two equinoxes, in early northern spring and fall. The ascending branch of the Hadley cells shifts according to the season, as the heating in the subsolar point moves over the planetary surface (Read
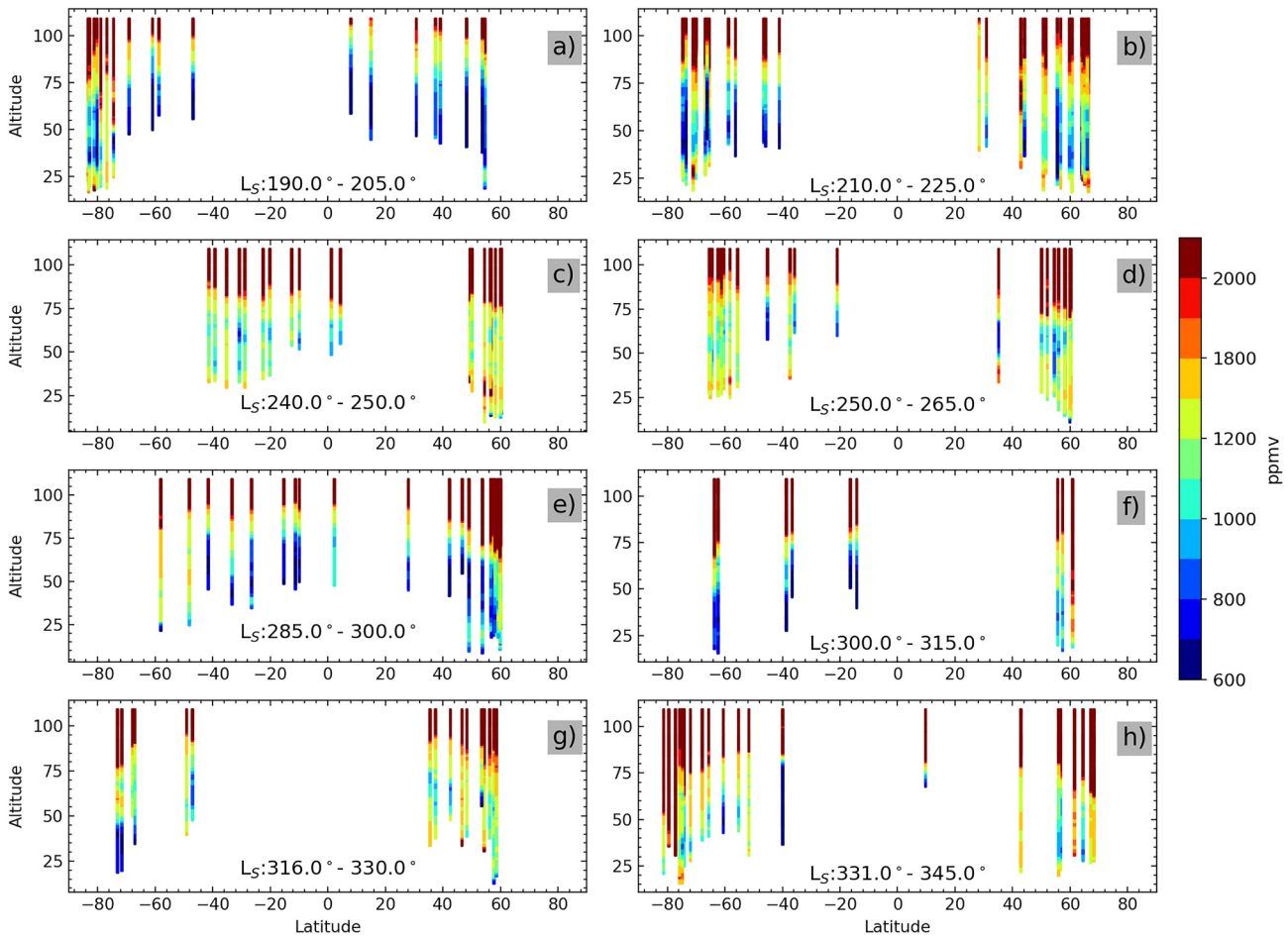
Figure 8. Latitudinal distribution of the retrieved CO profiles after grouping the results in 8 Ls intervals, as indicated in each panel. The color scale indicates the CO volume mixing ratio values in ppmv.

et al., 2015). During solstices, one of the Hadley branches becomes an intense cross-hemispheric cell, particularly strong during the southern summer solstice ($L_S = 270°–300°$) (Forget et al., 1999).

Each panel of Figures 8 and 9 corresponds to a fixed season indicated at the top of each panel. These eight periods include the onset of the dust storm ($L_S = 190°–205°$), the decaying phase of the GDS ($L_S = 210°–225°$), the initial phase of the perihelion season ($L_S = 240°–250°$), the late phase of perihelion ($L_S = 250°–265°$), and some periods of the southern summer ($L_S = 285°–300°$, $L_S = 300°–315°$, $L_S = 316°–330°$, and $L_S = 331°–345°$).

During the period $L_S = 190°–205°$ (Figures 8 and 9, panel a), the Martian dynamics is dominated by two Hadley cells increasing the CO mixing ratios at higher latitudes in both northern and SHs. In particular, the high mixing ratios found around 25 km over the southern polar latitudes seem to be the result of such a transport. A similar increase in CO VMR amount over the high northern latitudes has also been found by Olsen et al. (2021) during the equinox period.

As the season advances, the CO distributions in panels c–f show variations that can be related to slowly varying solar driven CO_2 photolysis at high altitudes (González-Galindo et al., 2009) and to a Hadley circulation pattern with an ascending flux which is evolving through these periods. The latitudinal gradient in the CO VMR above ~70 km vary with the seasons, as can be seen from the changes between panels. Around perihelion, the changes between adjacent panels c and d of Figures 8 and 9 are too short in time for a significant change in solar insolation. One possibility is that these are due to large scale transport. We cannot exclude also small scale variations, including measurement noise and thermal effects in the background atmosphere, for which CO VMR is very sensitive. At tropospheric altitudes, there are also changes which seem to be linked to water vapor. We know water
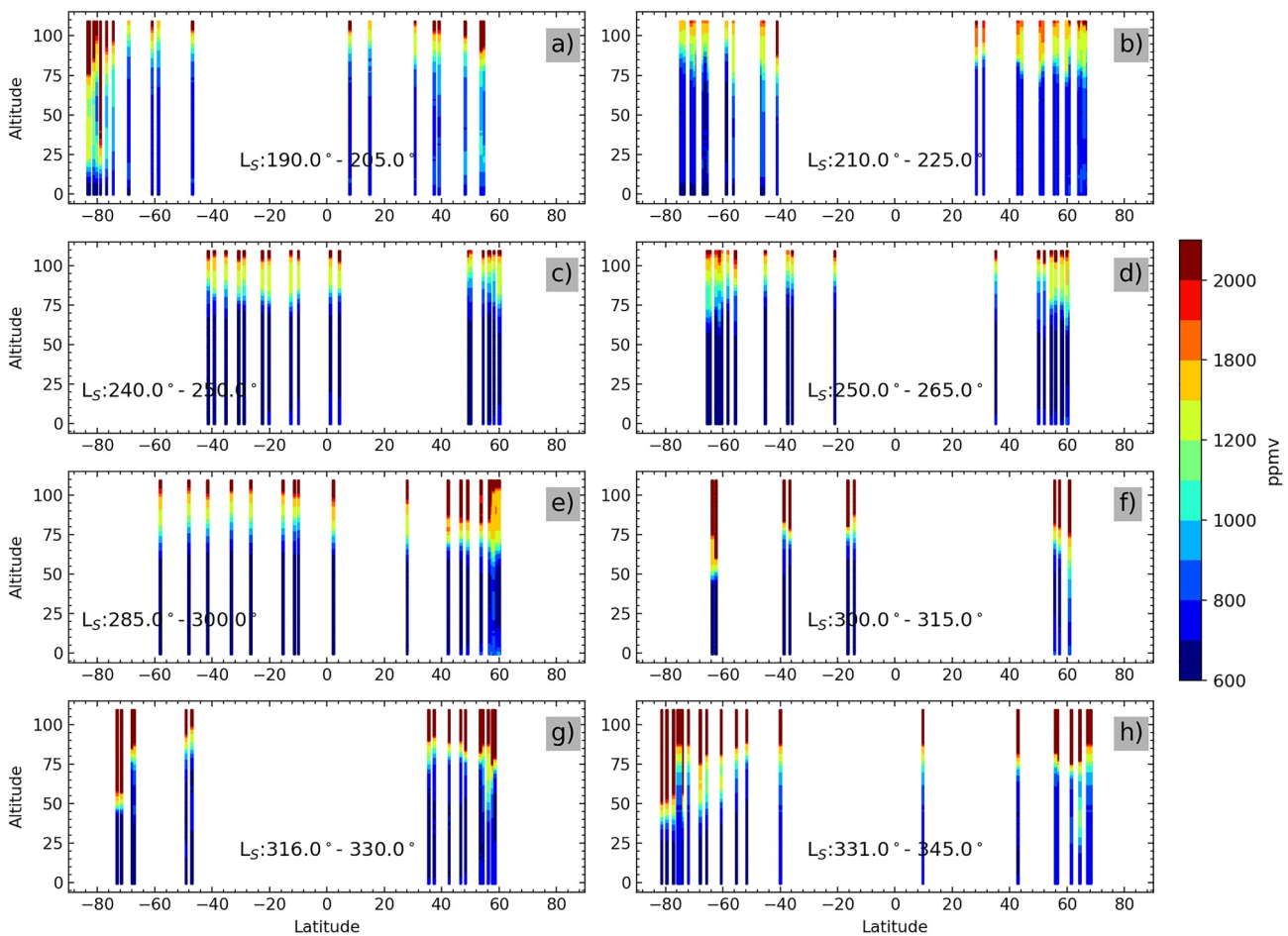
Figure 9. Latitudinal distribution as in Figure 8 but for the Planetary Climate Model CO, using the same set of 8 Ls intervals, as indicated in each panel. The color scale indicates the CO volume mixing ratio values in ppmv.

vapor presents significant variations in the lower atmosphere, and in particular in these seasons is lower than the amount observed during the GDS (Aoki et al., 2019; A. A. Fedorova et al., 2020; Brines et al., 2022). Unfortunately, we do not have homogeneous nor symmetric coverage in latitudes between both hemispheres during this key period that includes the perihelion and the southern summer solstice. CO seems to be an excellent tracer to characterize this season but more insightful analysis requires the use of GCM simulations or data assimilation.

During $L_S = 285°–300°$ and $L_S = 300°–315°$ (panels e and f in Figure 8), a fully developed global interhemispheric circulation can be seen in the CO distribution. The latitudinal coverage is patchy and we should rather claim that the distribution observed is compatible with such a global cross-hemispheric pattern, more neatly shown with model simulations (Daerden et al., 2019; Olsen et al., 2021). With this caution in mind, the downwelling branch in the NH seems to be at around 60°N and seems to reach down to lower tropospheric altitudes, 20–25 km, layers which seem to be enriched in CO compared to lower latitudes. We notice that during this season the distribution from the PCM shows a lower enrichment in CO, which indicates a weaker downwelling in the model. Over 60°N, downwelling of the PCM CO seems to reach only around altitude ∼55 km increasing the VMR values > 1,000 ppm while in the next panel (Figure 9, panel f), the downwelling seems to increase and reach the altitudes around 40 km and VMR values around ∼900 ppm.

At low altitudes, the TGO mapping is incomplete but low CO amounts are clearly observed at mid-low latitudes (50°S–50°N) from the beginning of the perihelion season (panel d in Figure 8). This low abundance is maintained or slightly increased during the southern summer (panels e–f). Later on, at the end of southern summer/northern fall, observations by TGO at higher latitudes were possible again (panels g and h in Figure 8). The CO abundance seems to increase there, possibly as a result of dynamics, following downwelling in both hemispheres. Also, the
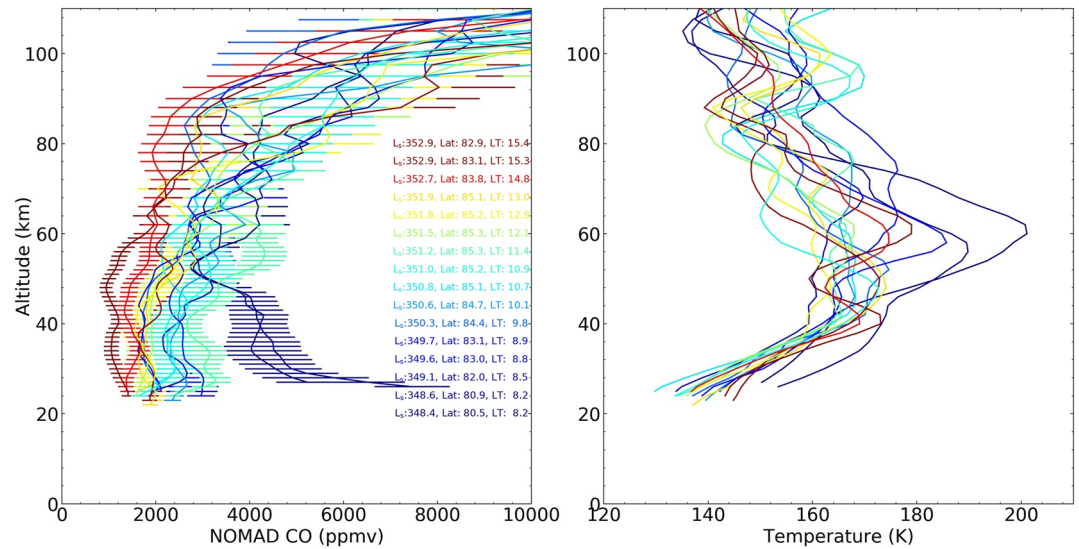
Figure 10. Left panel: variation of CO profiles with local time within a small latitudinal and seasonal box of ranges Lat = 80°–85° and L_S = 347°–353°. The color of the curves indicate the local time of the observations. Location and local time are indicated by the in-box text with the same color. Right panel: retrieved temperatures from Nadir and Occultation for Mars Discovery data associated to each of the CO profiles in the left panel. Temperatures below 20–25 km are not trusted due to low signal. See text for details.

amount of water vapor is decreasing, specially in the NH (A. Fedorova et al., 2021), which may add to the CO increase. In the period shown in panels g and h, we observe the largest CO over the North polar region. Such variations of the low altitude carbon monoxide cannot be seen in the PCM simulations (Figure 9). The PCM CO VMR between 20 and 40 km show small variations compared to that observed in the NOMAD SO observations.

5.3. Diurnal Variations

Given the mixtures of latitudes, seasons, and local times, it is not straightforward to separate them to highlight possible diurnal variations. The L_S spread of the morning (or the evening) observations over NH (see Figure 7a) are twice as long as the extent of these observations over SH (see Figure 7b). Also, note that for a given L_S range, NH observations are taken in the morning while SH observations are taken in the evening and vice-versa. We looked for locations where both latitude and L_S have small variations, but only found cases at very high latitudes. Here, we examine the retrieved profiles within the box indicated in Figure 7 panel a, which extends in L_S from 347° to 353° and in latitudes from 80°N to 86°N. The results are shown in Figure 10. Analysis of diurnal cycles at such high latitudes requires cautions, specially during equinox conditions, when the axial tilt is perpendicular to the sun. Trace mixing ratios in polar regions are very affected by global dynamics, hence some variations may not be necessarily diurnal. In addition, there can be an effect due to the L_S variation within our box because at very high latitudes and close to equinox, an L_S range of only 6° (about a week long) represents significant changes in the illumination conditions.

The CO VMR in Figure 10 shows a decrease with local time as well as with L_S below about 60 km. However, we cannot confirm this relation based only on this observation. As mentioned above the period of time described by this figure lies at the end of the northern polar night, approaching equinox. Therefore, most likely this variation is rather related to either downwelling within a polar vortex or to variations in the thermal structure or a combination of both. The polar vortex is particularly strong during Martian winter conditions but such an isolated region can also be formed near equinoxes (Mitchell et al., 2015; Streeter et al., 2021; Toigo et al., 2017). The decrease in the CO VMR with L_S may also indicate breaking of the polar vortex.

In Figure 10, we observe two peculiar profiles whose VMR values are quite large below about 45 km. These correspond to the latitudes 80.5°N and 80.9°N and, again, there are a few plausible explanations of this result, although none of them is completely satisfactory. One possibility is descending CO-rich air within a displaced polar vortex. However, the two locations might require the vortex to be split, as they are not closely placed, and
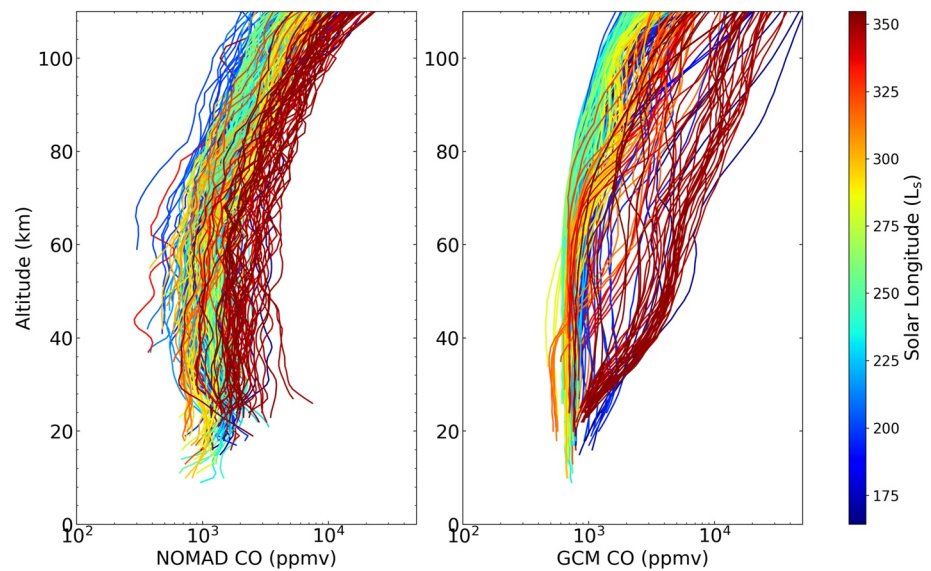
Figure 11. Comparison of the whole set of retrieved Nadir and Occultation for Mars Discovery CO volume mixing ratio profiles (left panel) with the Planetary Climate Model results (right-hand side panel). The color scale indicates the solar longitude of the scans.

this is not a common situation in Mars (Mitchell et al., 2015). A second possibility is associated to extremely cold patches, near the CO_2 condensation temperature. In such an instance, there should follow an increase in the relative abundance of CO. For this purpose we have examined the individual temperature and density profiles obtained from the NOMAD data by our team down to about 26 km (López Valverde et al., 2022). They are shown in the right panel of Figure 10. The retrieved temperature below about 20–25 km should not be trusted due to low signal (they are merged to the PCM a priori), but in the altitudes where the CO VMR is high, the temperatures are not particularly extreme, a result which certainly does not support this cold-patch hypothesis. Still, this does not completely rule out the possibility of a stronger CO_2 condensation in those two profiles because such process might happen at lower altitudes, near the Martian surface, which cannot be seen in our data. We should turn to a third possibility, which is some unknown bias in the inversion. This is not a fully satisfactory explanation either, since we do not observe any peculiarity in the residuals nor in the retrieval performance (convergence, AKs) of these two profiles. In our opinion, these peculiar CO VMR profiles demand more observations at high latitudes, analyzing NOMAD data collected during more Mars Years, which is an ongoing work in our team.

5.4. Comparison With PCM Simulation

Figures 11 and 12 show comparisons between the CO distribution from the Mars PCM and our retrieved values. For each NOMAD SO scan, a CO VMR profile was extracted from the model at the exact latitude, longitude, local time, and L_S of the occultation path at 50 km altitude, that is, approximately at the scan's midpoint.

Figure 11 shows the same trend in the vertical distribution of CO in both sets, with a relative abundance increasing with altitude. The scans are shown in colors following the solar longitude but without distinction among latitudes or hemispheres. This permits a quick visual realization of the global increase in CO VMR with season at high altitudes, between $L_S = 170°$ (blue profiles) and $L_S = 350°$ (dark red). However, in the NOMAD VMR, the vertical positive gradient is particularly strong above 60 km, while in the PCM some profiles present steep gradients also at tropospheric altitudes. The retrieved profiles show small scale variations consistent with the measurement noise but also larger oscillations not observed in the PCM data. Similar larger oscillations are also found in the retrieved temperature profiles (López Valverde et al., 2022) compared to the PCM values. We think this may indicate larger dynamical activity than in the model in the form of thermal tides and gravity waves.

Further insights into the NOMAD-PCM comparison can be obtained with Figure 12. This shows that the PCM global distribution and our retrievals agree well. Particularly, the seasonal behavior of the CO VMR above ~60 km is similar in both distributions. However, some differences can be seen and are highlighted next. First, the
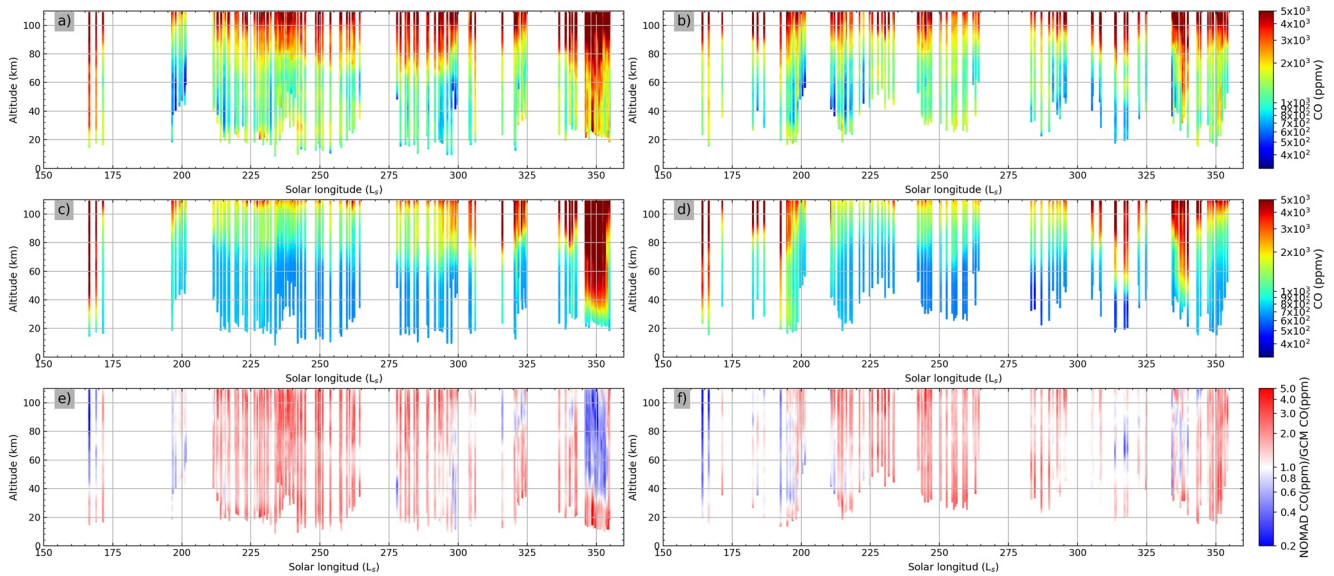
Figure 12. Comparison of Planetary Climate Model (PCM) CO densities with the retrieved ones. The top panels (a) and (b) show the retrieved CO volume mixing ratio. Panels (c) and (d) show the PCM CO mixing ratios and panels (e) and (f) show the ratios Nadir and Occultation for Mars Discovery/PCM. Left panels (a, c, and e) correspond to the NH and right panels (b, d, and f) to the SH.

PCM CO abundances are globally lower than the NOMAD retrievals at all altitudes, especially in the mesosphere (above 60 km). There are exceptions to this rule, especially at low altitudes, which are evident in Figure 11. Secondly, the two equinox periods show significant differences. During the northern autumn equinox period, $L_S = 160°$–$180°$, mixing ratios lower than the PCM are observed at high latitudes. A similar result was obtained by Olsen et al. (2021) from their model-data comparisons. The agreement between model and data seems better at lower-midlatitudes and in both hemispheres, although not many profiles are available in this period to support this idea. In the other equinox period, during $L_S = 345°$–$354°$, the retrieved CO is lower than the PCM in the NH by at least a factor of 2 while the opposite is observed in the SH.

Among other differences, the PCM maps do not show a depletion of CO during the onset and decay phases of the GDS as strong as in the NOMAD results. However, in this period, comparatively a better quantitative agreement is obtained between the a priori and the retrieved CO. The modeled water vapor and temperatures are also in better agreement with the retrieved water vapor (Brines et al., 2022) and the retrieved temperature (López Valverde et al., 2022). A last significant difference is observed around $L_S = 315°$ at altitudes between 60 and 80 km. This corresponds to southern high latitudes, where both distributions show a large CO abundance at mesospheric altitudes, driven by an active global circulation, but it is larger in the PCM by a factor 3–5.

6. Comparison With Previous Results

Figure 13 shows a comparison of our CO vertical profiles with the profiles retrieved from ACS observations (Olsen et al., 2021). The ACS and SO profiles observed within a box of 5° latitude and 5° L_S are chosen for the comparison. From the 32 profiles studied by Olsen et al. (2021), 17 were selected for this comparison. Since the ACS and SO observations are not exactly collocated and they are processed with two very different retrieval schemes, some differences in the CO densities are expected. Profiles in panels b–d show the CO densities during the onset of the GDS. The results from the both instruments compare well although our retrieved values are lower than those from ACS below 80 km. The average of the differences, in the range between the lowermost available altitude and 75 km, are 225 and 250 ppm in panel b, 306 ppm in panel c, and 308 ppm in panel d. During the high dust loading period, however, the average difference is lower, within 150–200 ppm (for panels e–j). The highest average difference can be seen over the northern high latitudes during the equinox and reaches 850–1,200 ppm (panel a).

A major difference among these profiles is to be noted above 80 km where an increase in VMR is usually observed due to photochemical production. Our values start to increase above 80 km whereas the ACS values
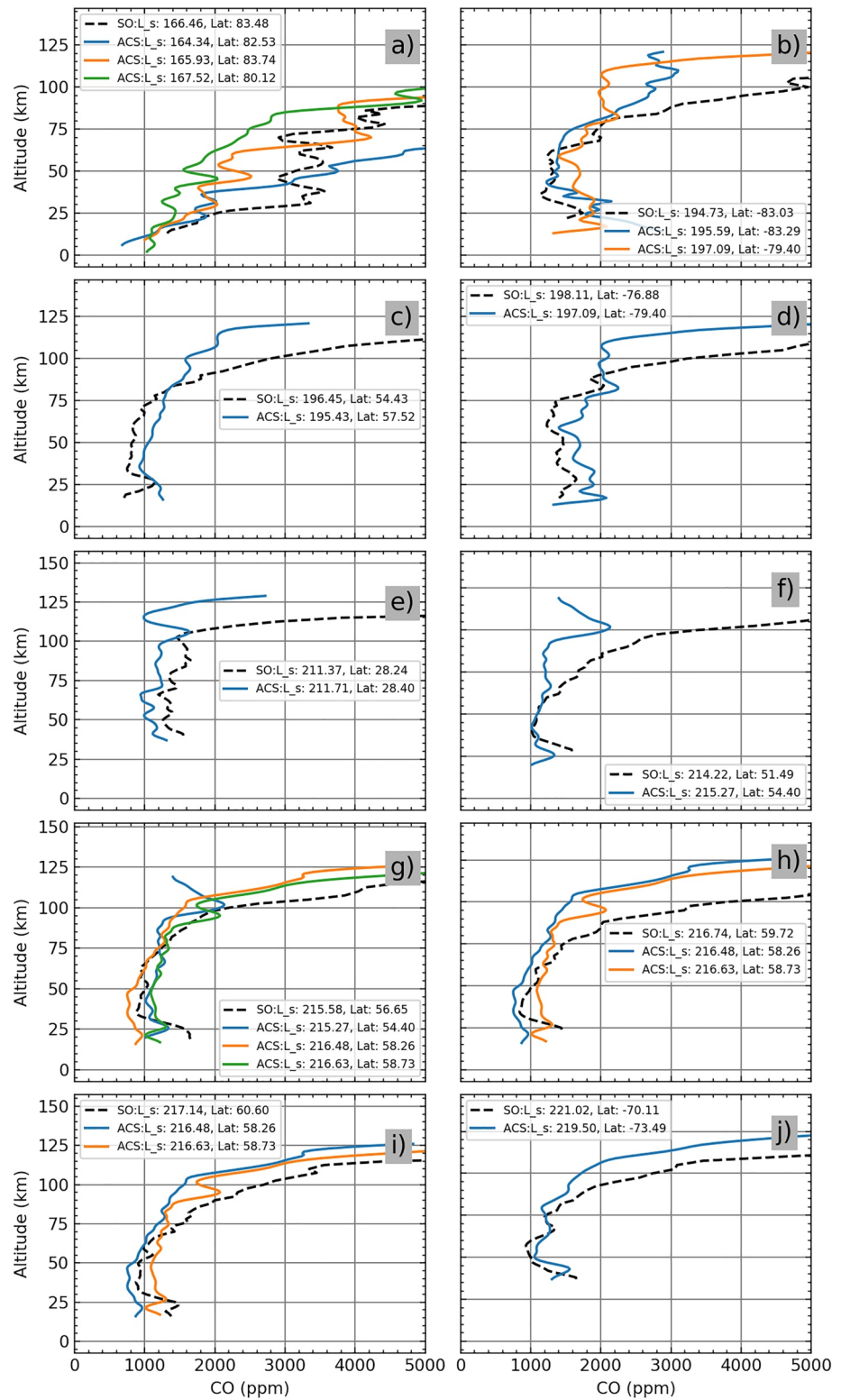
Figure 13. Comparison of the CO profiles in this study with the CO profiles obtained from Atmospheric Chemistry Suite observations (Olsen et al., 2021). The common profiles within the Lat-L_S box of dimension $5° × 5°$ are compared.

start increasing above 100 km. Let us recall that at these high altitudes, the measurements are particularly noisy, even in the temperature retrievals, and both ACS MIR and NOMAD SO present the largest uncertainties. Apart from these differences, and as mentioned above, our CO VMR results compare well with the ACS profiles, the differences between them arising most likely from different thermal structures and differences in retrieval methods. This is a first comparison intended to illustrate the need of a further, more in-depth, and coordinated comparison between both instruments.

Other instruments from the Mars orbit and ground-based observations have provided column abundances of CO. These columnar mixing ratios are obviously representative of the CO abundance near the planet's surface. In our retrieved profiles, the lowest altitude of sounding is variable depending on atmospheric dust loading, but is above 20 km in most solar occultation scans. The amount of CO in a column below our lowermost altitude is between 5 and 50 times the amount of CO above. In order to compare with previous nadir measurements, instead of CO column mixing ratios, we have calculated mean VMRs of our retrieved CO profiles. These are computed from the lowermost retrieved altitude up to 60 km, averaging these in the L_S bins of Figure 8 and comprising all the latitudes between 45°N and 45°S. The global average value obtained is 884 ppm. This compares well with LNO and PFS global averages, which are 800 ppm (Smith et al., 2021) and 820 ppm (Bouche et al., 2021), respectively. The global average values obtained from ACS NIR and MIR is 970 ppm (A. Fedorova et al., 2022) which is 9% higher than our values. Therefore, in terms of global averages, our VMRs are comparable with the previous results. During the GDS, however, we obtained a lower average VMR, of 619 ppm, while the LNO and PFS nadir data do not show this depletion. Both MIR and NIR also found an averaged depletion in this period. In another period that we analyzed, during the southern summer around $L_S = 270°–300°$, our values are around 900 ppm, which is higher than the column measurements by LNO and CRISM but agree well with NIR and MIR results. Our averaged binned values also seem to agree with NIR and MIR at the end of the MY34, with average VMR around 800–850 ppm.

7. Summary and Conclusions

For the first time, we have retrieved Martian CO density profiles up to about 100 km tangent altitudes from the NOMAD SO channel for MY 34 between $L_S = 160°–354°$ using collocated retrievals of temperatures and pressures. The two main sources of uncertainty in our results come from the variability in the AOTF transfer function and from the temperatures. The retrieval errors are typically lower than 10% below 80 km which can grow up to 30% above this altitude. Below 80 km the vertical resolution is usually better than 5 km.

The distribution of CO abundances observed by NOMAD globally agrees with latitudinal and seasonal variations obtained before with nadir observations, made by spacecraft instruments like CRISM (Smith et al., 2009), PFS (Sindoni et al., 2011), and NOMAD-LNO nadir sounding (Smith et al., 2021). Our retrieved CO mixing ratios agree well with the retrieved CO mixing ratios from ACS observations. The agreements are strikingly well during the onset and decay period of the GDS. The agreement with ACS results during the equinox period over northern high latitudes is also good regarding the sharp increase in VMR values with altitude, which was obtained with both the instruments (Figure 13).

We find a strong depletion in CO VMRs during the onset of GDS, which is more pronounced over the NH. This was also reported by Olsen et al. (2021), who mentioned a possible explanation related to the amount of H_2O. During the dust storm season, the atmospheric water vapor increases, and therefore the OH radicals, which causes this depletion. We think this may indeed be one of the reasons, and below we describe the period, southern summer, where we also observe links between the H_2O and CO abundances.

We observe an enhancement in CO at altitudes around 25 km over the SH during the onset of the GDS. We attribute this enhancement to the downwelling branch of the southern Hadley cell (bringing down mesospheric air, enriched in CO, as detailed in Section 5.2). However, a different increase in the CO densities is found over the northern hemisphere from low to midlatitudes during the decay phase of the GDS. In contrast to the previous one, this enhancement could rather be dominated by the lack of OH radicals following the decrease of incoming solar radiation.

The seasonal behavior of CO profiles reveals that CO VMRs below 60 km decrease during the southern summer all over the globe. This decrease may respond to a combination of effects. One of these can be the release of CO_2

and H_2O from the southern polar cap during this season (Forget et al., 2008). Increase of CO VMR at these altitudes is only found at the beginning of southern spring and the end of southern summer.

Regarding the latitudinal distribution, a couple of distinct periods can be seen in the data. In particular, the period $L_S = 285°–300°$ shows the impact of the global Hadley circulation. The descending branch of the global Hadley cell lies over 60°N, while the ascending branch is seen in the SH around 40°S. This describes well the known dynamical global pattern on Mars during the southern summer solstice $L_S = 270°–300°$ (Forget et al., 1999; Neary et al., 2020; Read et al., 2015).

Regarding the comparison with the Mars PCM (our a priori), the simulated CO VMRs agree qualitatively with the retrieved CO. A good quantitative agreement between the simulated and the observed CO VMRs is found during the onset of the GDS and during the period around $L_S = 300°$ when the modeled water vapor and temperature are also in better agreement with the retrieved values (Brines et al., 2022; López Valverde et al., 2022). Nonetheless, there are some significant differences. Among the differences with the PCM simulations, our retrieved CO VMR seems to be lower than the model prediction during the beginning of the northern spring over NH. In this season, the retrieved CO VMRs are larger over the SH. In general, the retrieved VMRs are higher than the simulated values during $L_S = 210°–290°$. An important difference was found in the comparison of the latitudinal distributions of CO (Figures 8 and 9), which is the presence of a weaker south-to-north transport in the model during the southern summer. The NOMAD SO profiles (Figure 8, panel e) show a larger enrichment of CO mixing ratios over the northern high latitude surely due to a stronger global Hadley cell.

We plan to extend our retrieval approach to the whole NOMAD data set in order to study CO distribution for a couple of complete Martian years to compare the CO mixing ratios between years with and without GDS and to gain further insight into seasonal and latitudinal variations in a more complete coverage. This data set can also be very valuable for GCM modeling and validation purposes. Detailed comparisons with ACS observations of CO are also foreseen.

Appendix A: AOTF Characterization

The Nadir and Occultation for Mars Discovery (NOMAD) solar occultation (SO) measurements are acquired by selecting different diffraction orders, and each data file corresponds to one order. This is because the Acousto Optical Tunable Filter (AOTF) ideally selects one order at a time for diffraction through the grating, and we call it the main diffraction order during that observation. The tuning of the AOTF for whichever main diffraction order is set through a radio-frequency input. A typical AOTF tuning relation with wavenumber is given in Neefs
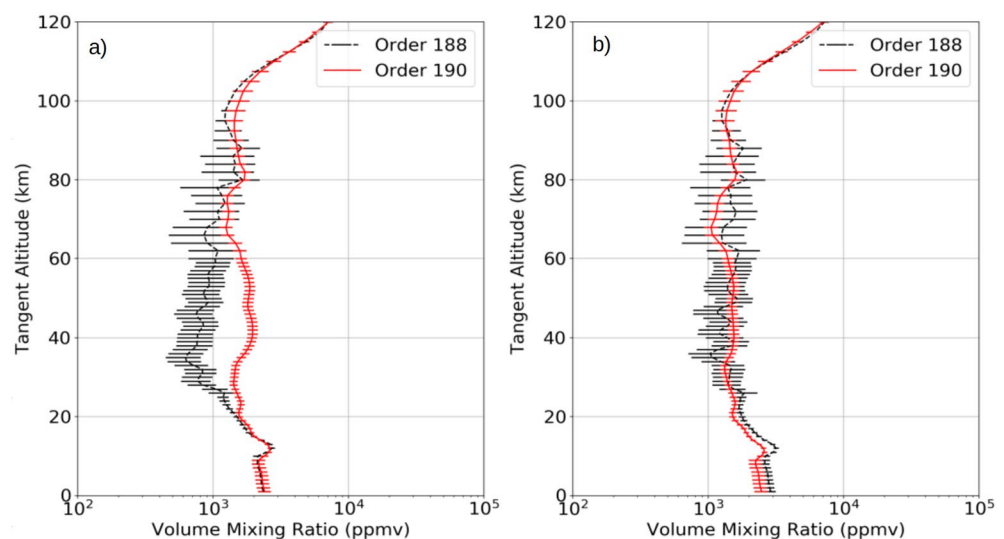

Figure A1. Agreement between the CO profiles from orders 188 and 190 before (panel a) and after (panel b) the fine-tuning of the Acousto Optical Tunable Filter parameters for scan *20180907_014655_1p0a_SO_A_I*. In these retrievals, a dust filter of opacity 0.5 has been applied which corresponds to an altitude ~18 km. This implies no use of measurement below the altitude.
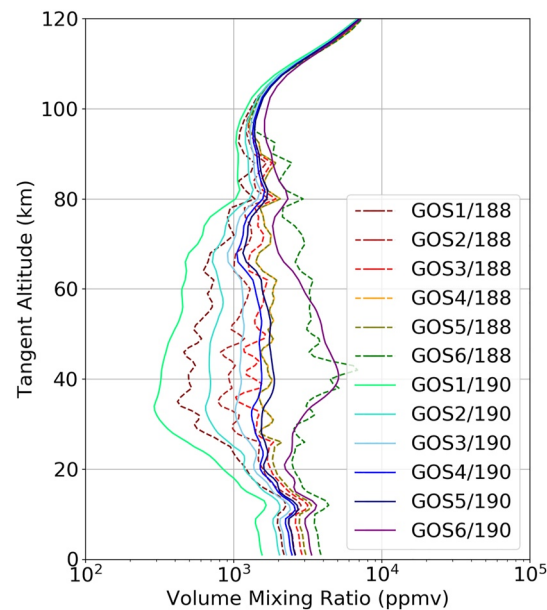
Figure A2. Response of the retrieved CO profiles to variations in the Gaussian offset. GOS1, GOS2, GOS3, GOS4, GOS5, and GOS6 correspond to values 0.1, 0.15, 0.18, 0.2, 0.3, and 0.35, respectively. The nominal Gaussian offset (GOS) is 0.2132 for order 190. See text for details.

et al. (2015). For example, for a radio frequency of 25 MHz, the diffraction order 190 is selected. The diffraction efficiency of the AOTF is characterized by a function over the permitted bandpass and is called AOTF transfer function (Liuzzi et al., 2019; I. Thomas et al., 2016). The precise functional of the AOTF is very important to characterize the measurement, and it has been the subject of a recent revision (Villanueva et al., 2022), which proposed an asymmetric sync-squared function characterized by four parameters. The functional and the parameters were determined using what are called miniscans, that is, a specific sun observation campaign devoted to fine-tune the channel calibration. As a result of that study, nominal values for those parameters were proposed for each of the NOMAD SO diffraction orders. However, the empirical characterization of the parameters is not perfect, and the uncertainties are particularly large in the spectral region of the CO orders 186–191.

For this reason, CO is one of the hardest targets of the NOMAD SO channel, and it requires a good fine-tuning of its AOTF. In order to gain some insight into this key analysis, we need to analyze further some of the AOTF parameters.

The sinc square AOTF function basically consists of a series of decreasing sidelobes around the main peak, this one laying in the main order while the sidelobes peak in the adjacent orders. The magnitude and shape of the sidelobes are parameterized with the help of an "asymmetry factor" (AF) and a "sidelobes ratio" (SR). As its name suggests, a larger SR increases the relative importance of the sidelobes and decreases the AOTF response in the central lobe, that is, in the main order. On the other hand, a large AF decreases the left lobes and introduces asymmetry between the lobes on both sides. For the detailed discussion on the AOTF parameters, we refer to Villanueva et al. (2022). Our AOTF also allows for a possible nonzero baseline component, which is parameterized as a shallow and wide Gaussian function, which in the spectral region of the CO orders is about 70.71 cm^{-1} wide and has a peak (referred to as Gaussian offset, or GOS hereafter) of 0.2132, for a normalized AOTF in the central lobe.

An extensive analysis using retrievals of full CO profiles was performed in order to fine-tune these parameters, following a perturbation study and looking for a minimization of the retrievals' residuals. For the evaluation of the residuals, we use the goodness of a fit as defined by a χ^2 value (Equation 3 in Section 4). In addition, the accurate determination of the AOTF parameters should result in similar carbon monoxide densities for different CO orders due to a more realistic contribution to the CO absorption lines from different orders.

Figure A1 (panel a) shows an example of a CO profile retrieved for one particular scan (*20180907_014655_1p0a_SO_A_I* taken at around 58°N and L$_s$~245°) where two different diffraction orders were measured at the same
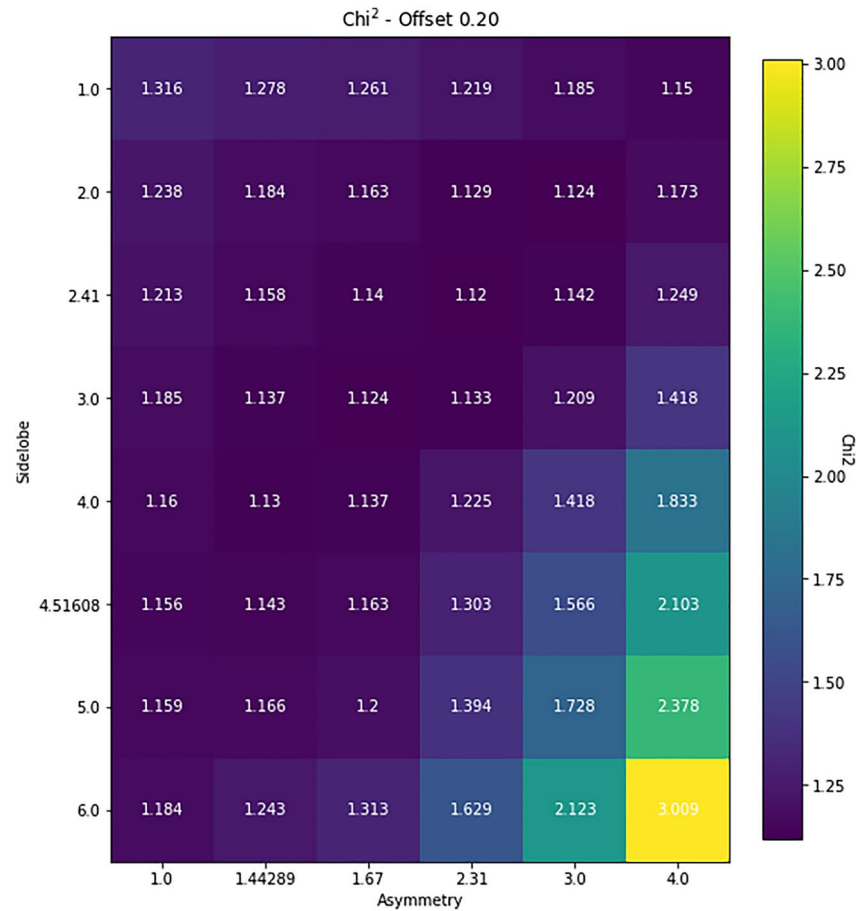
Figure A3. The χ^2 values tabulated for different values of sidelobe ratios and asymmetry factors (AFs). The color in the table indicate the values of the χ^2. The lowest χ^2 is obtained for a sidelobe ratio 2.41 and AF 2.31.

time, orders 188 and 190. In this retrieval, the nominal AOTF parameters were used. The overall agreement between these two CO profiles in the altitude region between 20 and 80 km is not very satisfactory.

In order to make the fine-tuning simple, we started with one of the parameters, in particular the Gaussian offset, or GOS. We chose only the central part of the CO orders, dominated by a relatively small number of CO absorption lines. In the center of a given order, the contribution from that main order is largest compared to other orders' contributions, and the GOS parameter plays the most important role in determining the total contribution (Villanueva et al., 2022). We also selected one scan with low to moderate measurement noise and confined our retrievals to altitudes with low dust opacity (*20180907_014655_1p0a_SO_A_I*, mentioned above). In this scan, a slant optical depth lower than 0.5 means altitudes above 18 km, approximately. We chose a set of values around the nominal value GOS = 0.2132 proposed by Villanueva et al. (2022) for order 190. Figure A2 shows a comparison among the vertical CO profiles obtained with six different GOS values. The CO volume mixing ratio (VMR) in the region between 30 and 80 km is very sensitive to this parameter. The lowest χ^2 was found for values within 0.1 and 0.2. A similar exercise is repeated for order 188. Values of 0.18 for order 188 and 0.2 for order 190 were finally selected as our best Gaussian offsets.

As for the other parameters namely, the AF and the SR, another extensive set of retrievals was performed, once the GOS values were fixed. A table of the χ^2 values obtained from their best fit residuals at the end of the inversions is presented in Figure A3. Similar analysis has been performed to fine-tuning other NOMAD SO orders by our team (see companion papers in this special issue). The closer the χ^2 value to unity the better the fitting of the retrieval (Jurado Navarro, 2016). In Figure A3, the region of this parameter space with best χ^2 values, shown in dark blue, occupies a broad diagonal. The values finally selected for this study lie in this diagonal correspond to SR = 2.41 and AF = 2.31.

Back to Figure A1, the CO VMR obtained with the fine-tuned parameters described here are shown in panel b. They are much closer than with the nominal values from Villanueva et al. (2022) and the differences lie within the errors of the retrieval. We recommend these values and AOTF for any future retrievals of CO from these NOMAD SO orders.

Appendix B: Synthetic Retrievals

Synthetic retrievals represent an excellent exercise to analyze the performance of a given retrieval setup and assumptions, like regularization and dependence on a priori climatologies. In this study, synthetic spectra were generated using our forward model Karlsruhe Optimized and Precise Radiative transfer Algorithm (KOPRA) and are intended to supply spectra equivalent to the Level 1 calibrated transmittances provided by the NOMAD PI team, but we used a given set of AOTF parameters, therefore avoiding uncertainties from the actual instrument's AOTF. For the same reason, these spectra are free from bending effects and from spectral shifts due to inaccuracies during calibration (see Section 3). The atmospheric pressure and temperature and the a priori CO were obtained from the Mars PCM model. The KOPRA simulations correspond to the precise altitudes of a given scan in order 190. A random noise component with a standard deviation given by the measurement noise in the calibrated data file was added to the KOPRA simulations.

In this section, we present a study devoted to test the dependence on the a priori CO densities. In Figure B1, we show three CO profiles, from retrievals performed with three different a priori CO profiles: (a) the nominal VMR from the GCM, which also represents the "true profile," (b) the nominal profile reduced by 50% at all altitudes, and (c) the nominal profile increased by 50% at all altitudes. In the three exercises, the retrieved CO densities essentially coincide among them and with the true profile, with deviations lower than the retrieval errors. Thus, in these conditions, our retrieval scheme gives correct and robust results against a priori assumptions.
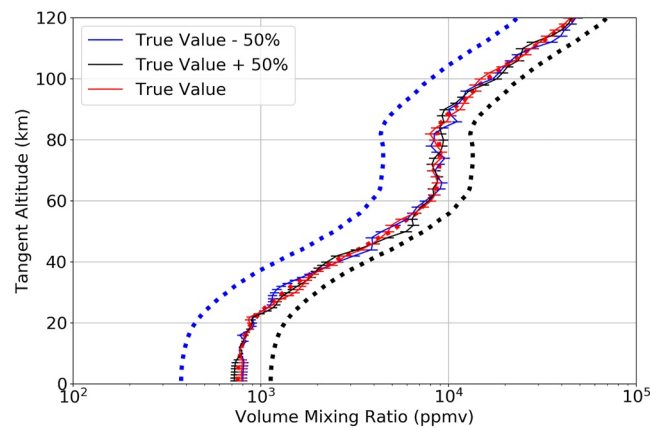

Figure B1. CO profiles retrieved from the synthetic transmittance generated with true value of CO. Colored solid line with error bar is the retrieved CO with an a priori indicated by the dotted line with same color.

Data Availability Statement

The HDF5 data files of NOMAD SO Level 1a transmittances used in this study are available at European Space Agency (ESA) planetary archive (https://archives.esac.esa.int/psa) and also at the NOMAD data center (https://nomad.aeronomie.be/index.php/data; I. R. Thomas et al., 2022; Vandaele et al., 2019). The retrieved results, presented in this work are archived at the zenodo repository and can be accessed from Ashimananda Modak (2022).

References

Alday, J., Trokhimovskiy, A., Irwin, P. G., Wilson, C. F., Montmessin, F., Lefèvre, F., et al. (2021). Isotopic fractionation of water and its photolytic products in the atmosphere of Mars. *Nature Astronomy*, *5*(9), 943–950. https://doi.org/10.1038/s41550-021-01389-x

Aoki, S., Daerden, F., Viscardy, S., Thomas, I., Erwin, J. T., Robert, S., et al. (2021). Annual appearance of hydrogen chloride on Mars and a striking similarity with the water vapor vertical distribution observed by tgo/nomad. *Geophysical Research Letters*, *48*(11), e2021GL092506. https://doi.org/10.1029/2021gl092506

Aoki, S., Vandaele, A. C., Daerden, F., Villanueva, G. L., Liuzzi, G., Thomas, I. R., et al. (2019). Water vapor vertical profiles on Mars in dust storms observed by TGO/NOMAD. *Journal of Geophysical Research: Planets*, *124*(12), 3482–3497. https://doi.org/10.1029/2019je006109

Belyaev, D. A., Fedorova, A. A., Trokhimovskiy, A., Alday, J., Montmessin, F., Korablev, O. I., et al. (2021). Revealing a high water abundance in the upper mesosphere of Mars with ACS onboard TGO. *Geophysical Research Letters*, *48*(10), e2021GL093411. https://doi.org/10.1029/2021gl093411

Billebaud, F., Brillet, J., Lellouch, E., Fouchet, T., Encrenaz, T., Cottini, V., et al. (2009). Observations of CO in the atmosphere of Mars with PFS onboard Mars Express. *Planetary and Space Science*, *57*(12), 1446–1457. https://doi.org/10.1016/j.pss.2009.07.004

Billebaud, F., Crovisier, J., Lellouch, E., Encrenaz, T., & Maillard, J. (1991). High-resolution infrared spectrum of CO on Mars: Evidence for emission lines. *Planetary and Space Science*, *39*(1–2), 213–218. https://doi.org/10.1016/0032-0633(91)90144-y

Bouche, J., Coheur, P.-F., Giuranna, M., Wolkenberg, P., Nardi, L., Amoroso, M., et al. (2021). Seasonal and spatial variability of carbon monoxide (CO) in the martian atmosphere from PFS/MEX observations. *Journal of Geophysical Research: Planets*, *126*(2), e2020JE006480. https://doi.org/10.1029/2020je006480

Brines, A., López-Valverde, M.-A., Stolzenbach, A., Modak, A., Funke, B., González-Galindo, F., et al. (2022). Water vapor vertical distribution on Mars during the perihelion season of MY34 and MY35 from ExoMars-TGO/NOMAD solar occultation measurements. *Journal of Geophysical Research: Planets*. https://doi.org/10.1029/2022je007273

Clancy, R., Muhleman, D., & Jakosky, B. (1983). Variability of carbon monoxide in the Mars atmosphere. *Icarus*, *55*(2), 282–301. https://doi.org/10.1016/0019-1035(83)90083-0

Clancy, R. T., Wolff, M. J., Whitney, B. A., Cantor, B. A., Smith, M. D., & McConnochie, T. H. (2010). Extension of atmospheric dust loading to high altitudes during the 2001 Mars dust storm: MGS TES limb observations. *Icarus*, *207*(1), 98–109. https://doi.org/10.1016/j.icarus.2009.10.011

Daerden, F., Neary, L., Viscardy, S., García Muñoz, A., Clancy, R., Smith, M., et al. (2019). Mars atmospheric chemistry simulations with the gem-Mars general circulation model. *Icarus*, *326*, 197–224. https://doi.org/10.1016/j.icarus.2019.02.030

Encrenaz, T., Fouchet, T., Melchiorri, R., Drossart, P., Gondet, B., Langevin, Y., et al. (2006). Seasonal variations of the martian CO over Hellas as observed by OMEGA/Mars express. *Astronomy & Astrophysics*, *459*(1), 265–270. https://doi.org/10.1051/0004-6361:20065586

Encrenaz, T., Lellouch, E., Gulkis, S., & Depater, I. (1991). Submillimeter observations of the (3-2) ^{12}CO and ^{13}CO transitions in the atmosphere of Mars. *Bulletin of the American Astronomical Society*, *23*, 1214.

Fedorova, A., Montmessin, F., Korablev, O., Lefèvre, F., Trokhimovskiy, A., & Bertaux, J.-L. (2021). Multi-annual monitoring of the water vapor vertical distribution on Mars by SPICAM on Mars express. *Journal of Geophysical Research: Planets*, *126*(1), e2020JE006616. https://doi.org/10.1029/2020je006616

Fedorova, A., Trokhimovskiy, A., Lefèvre, F., Olsen, K. S., Korablev, O., Montmessin, F., et al. (2022). Climatology of the CO vertical distribution on Mars based on ACS TGO measurements. *Journal of Geophysical Research: Planets*, *127*(9), e2022JE007195. https://doi.org/10.1029/2022je007195

Fedorova, A. A., Montmessin, F., Korablev, O., Luginin, M., Trokhimovskiy, A., Belyaev, D. A., et al. (2020). Stormy water on Mars: The distribution and saturation of atmospheric water during the dusty season. *Science*, *367*(6475), 297–300. https://doi.org/10.1126/science.aay9522

Forget, F., Hourdin, F., Fournier, R., Hourdin, C., Talagrand, O., Collins, M., et al. (1999). Improved general circulation models of the Martian atmosphere from the surface to above 80 km. *Journal of Geophysical Research*, *104*(E10), 24155–24175. https://doi.org/10.1029/1999je001025

Forget, F., Millour, E., Bierjon, A., Delavois, A., Fan, S., Lange, L., et al. (2022). Challenges in Mars climate modelling with the LMD Mars global climate model, now called the Mars "planetary climate model" (pcm). In *Seventh international workshop on the mars atmosphere: Modelling and observations* (p. 1102).

Forget, F., Millour, E., Montabone, L., & Lefevre, F. (2008). Non condensable gas enrichment and depletion in the Martian polar regions. In *LPI Contribution* (Vol. 1447, p. 9106).

González-Galindo, F., Forget, F., López-Valverde, M., Angelats i Coll, M., & Millour, E. (2009). A ground-to-exosphere Martian general circulation model: 1. Seasonal, diurnal, and solar cycle variation of thermospheric temperatures. *Journal of Geophysical Research*, *114*(E4), E04001. https://doi.org/10.1029/2008je003246

González-Galindo, F., López-Valverde, M., Angelats i Coll, M., & Forget, F. (2005). Extension of a Martian general circulation model to thermospheric altitudes: Uv heating and photochemical models. *Journal of Geophysical Research*, *110*(E9), E09008. https://doi.org/10.1029/2004je002312

Gordon, I. E., Rothman, L. S., Hill, C., Kochanov, R. V., Tan, Y., Bernath, P. F., et al. (2017). The HITRAN2016 molecular spectroscopic database. *Journal of Quantitative Spectroscopy and Radiative Transfer*, *203*, 3–69. https://doi.org/10.1016/j.jqsrt.2017.06.038

Guzewich, S. D., Lemmon, M., Smith, C., Martínez, G., de Vicente-Retortillo, Á., Newman, C., et al. (2019). Mars Science Laboratory observations of the 2018/Mars year 34 global dust storm. *Geophysical Research Letters*, *46*(1), 71–79. https://doi.org/10.1029/2018gl080839

Hess, S. L., Henry, R. M., & Tillman, J. E. (1979). The seasonal variation of atmospheric pressure on Mars as affected by the south polar cap. *Journal of Geophysical Research*, *84*(B6), 2923–2927. https://doi.org/10.1029/jb084ib06p02923

Höpfner, M., & Emde, C. (2005). Comparison of single and multiple scattering approaches for the simulation of limb-emission observations in the mid-ir. *Journal of Quantitative Spectroscopy and Radiative Transfer*, *91*(3), 275–285. https://doi.org/10.1016/j.jqsrt.2004.05.066

Jurado Navarro, Á. A. (2016). Retrieval of CO_2 and collisional parameters from the MIPAS spectra in the earth atmosphere.

Kakar, R., Walters, J., & Wilson, W. (1977). Mars: Microwave detection of carbon monoxide. *Science*, *196*(4294), 1090–1091. https://doi.org/10.1126/science.196.4294.1090

Kaplan, L. D., Connes, J., & Connes, P. (1969). Carbon monoxide in the Martian atmosphere. *The Astrophysical Journal*, *157*, L187. https://doi.org/10.1086/180416

Krasnopolsky, V. A. (1995). Uniqueness of a solution of a steady state photochemical problem: Applications to Mars. *Journal of Geophysical Research*, *100*(E2), 3263–3276. https://doi.org/10.1029/94je03283

Krasnopolsky, V. A. (2003). Spectroscopic mapping of Mars co mixing ratio: Detection of north-south asymmetry. *Journal of Geophysical Research*, *108*(E2), 5010. https://doi.org/10.1029/2002je001926

Krasnopolsky, V. A. (2015). Variations of carbon monoxide in the martian lower atmosphere. *Icarus*, *253*, 149–155. https://doi.org/10.1016/j.icarus.2015.03.006

Lefèvre, F., & Krasnopolsky, V. (2017). Atmospheric photochemistry. In *The atmosphere and climate of Mars* (Vol. 18, p. 405).

Lefèvre, F., Trokhimovskiy, A., Fedorova, A., Baggio, L., Lacombe, G., Määttänen, A., et al. (2021). Relationship between the ozone and water vapor columns on Mars as observed by SPICAM and calculated by a global climate model. *Journal of Geophysical Research: Planets*, *126*(4), e2021JE006838. https://doi.org/10.1029/2021je006838

Lellouch, E., Paubert, G., & Encrenaz, T. (1991). Mapping of co millimeter-wave lines in Mars' atmosphere: The spatial variability of carbon monoxide on Mars. *Planetary and Space Science*, *39*(1–2), 219–224. https://doi.org/10.1016/0032-0633(91)90145-z

Liuzzi, G., Villanueva, G. L., Mumma, M. J., Smith, M. D., Daerden, F., Ristic, B., et al. (2019). Methane on Mars: New insights into the sensitivity of CH_4 with the NOMAD/exoMars spectrometer through its first in-flight calibration. *Icarus*, *321*, 671–690. https://doi.org/10.1016/j.icarus.2018.09.021

López Valverde, M.-A., Funke, B., Brines, A., Stolzenbach, A., Modak, A., Hill, B., et al. (2022). Martian atmospheric temperature and density profiles during the 1st year of NOMAD/TGO solar occultation measurements. *Journal of Geophysical Research: Planets*, e2022JE007278. https://doi.org/10.1029/2022je007278

McElroy, M. B., & Donahue, T. M. (1972). Stability of the martian atmosphere. *Science*, *177*(4053), 986–988. https://doi.org/10.1126/science.177.4053.986

Mitchell, D., Montabone, L., Thomson, S., & Read, P. (2015). Polar vortices on Earth and Mars: A comparative study of the climatology and variability from reanalyses. *Quarterly Journal of the Royal Meteorological Society*, *141*(687), 550–562. https://doi.org/10.1002/qj.2376

Modak, A. (2022). Retrieval of Martian atmospheric CO vertical profiles from NOMAD observations during the 1st year of TGO operations measurements. *Zenodo*. https://doi.org/10.5281/zenodo.7268447

Modak, A., Sheel, V., & Lefèvre, F. (2020). Competing pathways in odd oxygen photochemistry of the martian atmosphere. *Planetary and Space Science*, *181*, 104783. https://doi.org/10.1016/j.pss.2019.104783

Montabone, L., Forget, F., Millour, E., Wilson, R., Lewis, S., Cantor, B., et al. (2015). Eight-year climatology of dust optical depth on Mars. *Icarus*, *251*, 65–95. https://doi.org/10.1016/j.icarus.2014.12.034

Montabone, L., Spiga, A., Kass, D. M., Kleinböhl, A., Forget, F., & Millour, E. (2020). Martian year 34 column dust climatology from Mars climate sounder observations: Reconstructed maps and model simulations. *Journal of Geophysical Research: Planets*, *125*(8), e2019JE006111. https://doi.org/10.1029/2019je006111

Navarro, T., Madeleine, J.-B., Forget, F., Spiga, A., Millour, E., Montmessin, F., & Määttänen, A. (2014). Global climate modeling of the Martian water cycle with improved microphysics and radiatively active water ice clouds. *Journal of Geophysical Research: Planets*, *119*(7), 1479–1495. https://doi.org/10.1002/2013je004550

Neary, L., & Daerden, F. (2018). The gem-Mars general circulation model for Mars: Description and evaluation. *Icarus*, *300*, 458–476. https://doi.org/10.1016/j.icarus.2017.09.028

Neary, L., Daerden, F., Aoki, S., Whiteway, J., Clancy, R. T., Smith, M., et al. (2020). Explanation for the increase in high-altitude water on Mars observed by nomad during the 2018 global dust storm. *Geophysical Research Letters*, *47*(7), e2019GL084354. https://doi.org/10.1029/2019gl084354

Neefs, E., Vandaele, A. C., Drummond, R., Thomas, I. R., Berkenbosch, S., Clairquin, R., et al. (2015). NOMAD spectrometer on the exoMars trace gas orbiter mission: Part 1—Design, manufacturing and testing of the infrared channels. *Applied Optics*, *54*(28), 8494–8520. https://doi.org/10.1364/ao.54.008494

Olsen, K., Lefèvre, F., Montmessin, F., Fedorova, A., Trokhimovskiy, A., Baggio, L., et al. (2021). The vertical structure of CO in the Martian atmosphere from the exoMars trace gas orbiter. *Nature Geoscience*, *14*(2), 67–71. https://doi.org/10.1038/s41561-020-00678-w

Parkinson, T., & Hunten, D. (1972). Spectroscopy and Acronomy of O_2 on Mars. *Journal of the Atmospheric Sciences*, *29*(7), 1380–1390. https://doi.org/10.1175/1520-0469(1972)029<1380:saaooo>2.0.co;2

Patel, M. R., Antoine, P., Mason, J., Leese, M., Hathi, B., Stevens, A. H., et al. (2017). NOMAD spectrometer on the exoMars trace gas orbiter mission: Part 2—Design, manufacturing, and testing of the ultraviolet and visible channel. *Applied Optics*, *56*(10), 2771–2782. https://doi.org/10.1364/ao.56.002771

Read, P., Lewis, S., & Mulholland, D. (2015). The physics of Martian weather and climate: A review. *Reports on Progress in Physics*, *78*(12), 125901. https://doi.org/10.1088/0034-4885/78/12/125901

Rodgers, C. D. (2000). *Inverse methods for atmospheric sounding: Theory and practice* (Vol. 2). World scientific.

Rodrigo, R., Garcia-Alvarez, E., Lopez-Gonzalez, M., & Lopez-Moreno, J. (1990). A nonsteady one-dimensional theoretical model of Mars' neutral atmospheric composition between 30 and 200 km. *Journal of Geophysical Research*, *95*(B9), 14795–14810. https://doi.org/10.1029/90jb00158

Schreier, F., Milz, M., Buehler, S. A., & von Clarmann, T. (2018). Intercomparison of three microwave/infrared high resolution line-by-line radiative transfer codes. *Journal of Quantitative Spectroscopy and Radiative Transfer*, *211*, 64–77. https://doi.org/10.1016/j.jqsrt.2018.02.032

Shaposhnikov, D. S., Medvedev, A. S., Rodin, A. V., & Hartogh, P. (2019). Seasonal water "pump" in the atmosphere of maMarsVertical transport to the thermosphere. *Geophysical Research Letters*, *46*(8), 4161–4169. https://doi.org/10.1029/2019gl082839

Sindoni, G., Formisano, V., & Geminale, A. (2011). Observations of water vapour and carbon monoxide in the martian atmosphere with the SWC of PFS/mex. *Planetary and Space Science*, *59*(2–3), 149–162. https://doi.org/10.1016/j.pss.2010.12.006

Smith, M. D., Daerden, F., Neary, L., & Khayat, A. (2018). The climatology of carbon monoxide and water vapor on Mars as observed by CRISM and modeled by the gem-Mars general circulation model. *Icarus*, *301*, 117–131. https://doi.org/10.1016/j.icarus.2017.09.027

Smith, M. D., Daerden, F., Neary, L., Khayat, A. S., Holmes, J. A., Patel, M. R., et al. (2021). The climatology of carbon monoxide on Mars as observed by NOMAD nadir-geometry observations. *Icarus*, *362*, 114404. https://doi.org/10.1016/j.icarus.2021.114404

Smith, M. D., Wolff, M. J., Clancy, R. T., & Murchie, S. L. (2009). Compact reconnaissance imaging spectrometer observations of water vapor and carbon monoxide. *Journal of Geophysical Research*, *114*(E2), E00D03. https://doi.org/10.1029/2008je003288

Sprague, A., Boynton, W., Kerry, K., Janes, D., Hunten, D., Kim, K., et al. (2004). Mars' south polar ar enhancement: A tracer for south polar seasonal meridional mixing. *Science*, *306*(5700), 1364–1367. https://doi.org/10.1126/science.1098496

Stiller, G. P. (2000). The Karlsruhe optimized and precise radiative transfer algorithm (KOPRA).

Streeter, P. M., Lewis, S. R., Patel, M. R., Holmes, J. A., Fedorova, A. A., Kass, D. M., & Kleinböhl, A. (2021). Asymmetric impacts on Mars' polar vortices from an equinoctial global dust storm. *Journal of Geophysical Research: Planets*, *126*(5), e2020JE006774. https://doi.org/10.1029/2020je006774

Thomas, I., Vandaele, A., Robert, S., Neefs, E., Drummond, R., Daerden, F., et al. (2016). Optical and radiometric models of the NOMAD instrument part ii: The infrared channels-SO and LNO. *Optics Express*, *24*(4), 3790–3805. https://doi.org/10.1364/oe.24.003790

Thomas, I. R., Aoki, S., Trompet, L., Robert, S., Depiesse, C., Willame, Y., et al. (2022). Calibration of NOMAD on ESA'S exomars trace gas orbiter: Part 1—The solar occultation channel. *Planetary and Space Science*, *218*, 105411. https://doi.org/10.1016/j.pss.2021.105411

Toigo, A., Waugh, D. W., & Guzewich, S. D. (2017). What causes Mars' annular polar vortices? *Geophysical Research Letters*, *44*(1), 71–78. https://doi.org/10.1002/2016gl071857

Vandaele, A. C., Korablev, O., Daerden, F., Aoki, S., Thomas, I. R., Altieri, F., et al. (2019). Martian dust storm impact on atmospheric H_2O and D/H observed by exomars trace gas orbiter. *Nature*, *568*(7753), 521–525. https://doi.org/10.1038/s41586-019-1097-3

Vandaele, A. C., Lopez-Moreno, J.-J., Patel, M. R., Bellucci, G., Daerden, F., Ristic, B., et al. (2018). NOMAD, an integrated suite of three spectrometers for the exoMars trace gas mission: Technical description, science objectives and expected performance. *Space Science Reviews*, *214*(5), 1–47. https://doi.org/10.1007/s11214-018-0517-2

Vandaele, A. C., Willame, Y., Depiesse, C., Thomas, I. R., Robert, S., Bolsée, D., et al. (2015). Optical and radiometric models of the NOMAD instrument part I: The UVIS channel. *Optics Express*, *23*(23), 30028–30042. https://doi.org/10.1364/oe.23.030028

Villanueva, G. L., Liuzzi, G., Aoki, S., Stone, S. W., Brines, A., Thomas, I. R. (2022). The deuterium isotopic ratio of water released from the Martian caps as measured with TGO/NOMAD. *Geophysical Research Letters*, *49*(12), e2022GL098161. https://doi.org/10.1029/2022gl098161

Villanueva, G. L., Liuzzi, G., Crismani, M. M., Aoki, S., Vandaele, A. C., Daerden, F., et al. (2021). Water heavily fractionated as it ascends on Mars as revealed by exomars/nomad. *Science Advances*, *7*(7), eabc8843. https://doi.org/10.1126/sciadv.abc8843

von Clarmann, T., Glatthor, N., Grabowski, U., Höpfner, M., Kellmann, S., Kiefer, M., & López-Puertas, M. (2003). Retrieval of temperature and tangent altitude pointing from limb emission spectra recorded from space by the Michelson Interferometer for Passive Atmospheric Sounding (MIPAS). *Journal of Geophysical Research*, *108*(D23), 4736. https://doi.org/10.1029/2003jd003602

Yoshida, N., Nakagawa, H., Aoki, S., Erwin, J., Vandaele, A. C., Daerden, F., et al. (2022). Variations in vertical CO/CO_2 profiles in the martian mesosphere and lower thermosphere measured by the exomars TGO/NOMAD: Implications of variations in eddy diffusion coefficient. *Geophysical Research Letters*, *49*(10), e2022GL098485. https://doi.org/10.1029/2022gl098485